JOURNAL OF GEOPHYSICAL RESEARCH, VOL. 112, D10116, doi:10.1029/2006JD008105, 2007

Retrieving surface parameters for climate models from Moderate Resolution Imaging Spectroradiometer (MODIS)-Multiangle Imaging Spectroradiometer (MISR) albedo products

B. Pinty,[1] T. Lavergne,[1] M. Voßbeck,[2] T. Kaminski,[2] O. Aussedat,[1] R. Giering,[2] N. Gobron,[1] M. Taberner,[1] M. M. Verstraete,[1] and J.-L. Widlowski[1]

Received 5 October 2006; revised 17 January 2007; accepted 21 January 2007; published 24 May 2007.

[1] We present a computer-efficient software package enabling us to assimilate operational remote-sensing flux products into a state-of-the-art two-stream radiation transfer scheme suitable for climate models. This package implements the adjoint and Hessian codes, generated using automatic differentiation techniques, of a cost function balancing (1) the deviation from the a priori knowledge on the model parameter values and (2) the misfit between the observed remote-sensing fluxes and the two-stream model simulations. The individual weights of these contributions are specified notably via covariance matrices of the uncertainties in the a priori knowledge on the model parameters and the measurements. The proposed procedure delivers a Gaussian approximation of the PDFs of the retrieved model parameter values. The a posteriori covariance matrix is further exploited to evaluate, in turn, the posterior probability density functions of the radiant fluxes simulated by the two-stream model, including those that are not measured, for example, the fraction of radiation absorbed in the ground. Applications are conducted using Moderate Resolution Imaging Spectroradiometer (MODIS) and Multiangle Imaging Spectroradiometer (MISR) broadband surface albedo products. It turns out that the differences between these two albedo sets may translate into discernible signatures on some retrieved model parameters. Meanwhile, adding the Joint Research Centre (JRC)-Fraction of Absorbed Photosynthetically Active Radiation (FAPAR) Sea-viewing Wide Field-of-view Sensor (SeaWiFS) products into the measurements yields a significant reduction of uncertainties. Results from these applications indicate that the products retrieved from the two-stream inversion procedure (1) exhibit much less variability than those generated by the operational algorithms for the LAI and FAPAR, and (2) are in good agreement with the available ground-based estimates.

Citation: Pinty, B., T. Lavergne, M. Voßbeck, T. Kaminski, O. Aussedat, R. Giering, N. Gobron, M. Taberner, M. M. Verstraete, and J.-L. Widlowski (2007), Retrieving surface parameters for climate models from Moderate Resolution Imaging Spectroradiometer (MODIS)-Multiangle Imaging Spectroradiometer (MISR) albedo products, *J. Geophys. Res.*, *112*, D10116, doi:10.1029/2006JD008105.

1. Introduction

[2] The availability from various institutions of global multiannual time series of surface products derived from space-borne sensors operating in the solar domain incites considering their genuine use in climate and large-scale models. A number of steps are, however, required to favor the systematic ingestion or assimilation of the remote-sensing products by these models. Those steps include, at least, (1) the assessment of the variability between products available from different sources which requires performing product intercomparison exercises [e.g., *Pinty et al.*, 2004b], (2) the evaluation of the absolute accuracy on the retrievals implying, whenever possible, joint analyses of the remote-sensing and the ground-based estimates [e.g., *Jin et al.*, 1999; *Shabanov et al.*, 2003; *Gobron et al.*, 2006], (3) the verification that the remote-sensing products actually fit the needs and expectations of the large-scale models regarding the spatial and temporal coverage [*Moody et al.*, 2005] which suggest achieving the fusion of products delivered by multiple sources when the former are shown to be indiscernible [*Salomon et al.*, 2006], (4) the evaluation of the performances of the land surface radiation schemes currently implemented in large-scale models that may now require intensive benchmarking against more sophisticated tools [e.g., *Anisimov and Fukshansky*, 1992; *Yang et al.*, 2001; *Niu and Yang*, 2004; *Wang*, 2005; *Pinty et al.*, 2006], and (5) the availability of advanced and computer-efficient

[1]Global Environment Monitoring Unit, European Commission, DG Joint Research Centre, Institute for Environment and Sustainability, Ispra (VA), Italy.
[2]FastOpt, Hamburg, Germany.

0148-0227/07/2006JD008105$09.00

assimilation procedures to facilitate the interfacing between the surface products measured from space and the corresponding quantities generated or required by land surface schemes. Results from preliminary attempts at addressing the first three items mentioned previously are encouraging enough, so that items 4 and 5 are becoming fully relevant topics to address.

[3] The three surface products retrieved from remote-sensing techniques that are of concern here are as follows: (1) the fraction of the radiant flux scattered by the surface, namely, the albedo in the broadband visible (0.3–0.7 μm) and near-infrared (0.7–3.0 μm) spectral domains, (2) the fraction of the radiant flux absorbed by the green part of vegetation canopies in the broadband visible domain, namely, the Fraction of Absorbed Photosynthetically Active Radiation (FAPAR), and (3) a state variable of the vegetation canopy, namely, the Leaf Area Index (LAI). Such products are derived from series of instruments operated by major space agencies and are available from various sources (see, for instance, http://envisat.esa.int, http://eosweb.larc.nasa.gov/, http://edcdaac.usgs.gov/, http://www.eumetsat.int/, and http://fapar.jrc.it/). These three surface products are of high relevance for analyzing and simulating exchange processes of energy and mass occurring through the upper and lower boundaries of a vegetation canopy layer.

[4] Revisiting the characteristics and performances of land surface radiation schemes currently implemented in climate and large-scale models must ideally meet numerous technical constraints (like computer efficiency and robustness, limited implementation, and maintenance costs) and scientific constraints (such as reaching simulation accuracy for radiant fluxes at least comparable, although ideally an order of magnitude better, to that associated with the retrieved estimates from remote sensing). The corresponding efforts should thus take place on at least two complementary fronts: (1) updating and eventually modifying the current radiation schemes in the vegetation layer to make them easy to couple, without dramatic increase in software maintenance cost, with the multilayer representation of the atmosphere and soil systems, and (2) improving the capability to represent reliably the effects due to the unresolved internal variability (along the horizontal and vertical directions) of the land surface properties such as, for instance, the leaf area density.

[5] Accounting for the three-dimensional effects due to vegetation clumping and tree structure in large-scale models is at the core of the problem to be solved. So far, indeed, the most advanced representation of the interactions between the solar radiation and vegetation canopy attributes relies on solutions, sometimes approximate, derived from one-dimensional approaches. Steps have been taken to propose alternate, mostly hybrid, solutions recognizing the importance of the departure from horizontal homogeneity which translates into significant modifications of the downward transmitted, upward scattered, and hence finally absorbed, radiant fluxes in the vegetation layer and the soil underneath. Since the two latter fluxes are those estimated operationally from space-borne sensor measurements, large-scale models will be able to fully capitalize on these estimations only to the extent that (1) they adequately represent the three-dimensional effects generated by the internal variability prevailing inside the vegetation layer and 2) the required information to simulate/parameterize this internal variability is available in some ways.

[6] *Pinty et al.* [2006] have shown that the two-stream representation used to simulate the radiant fluxes in vegetation layers at low spatial resolution is always capable of mimicking three-dimensional induced effects provided that effective (instead of true) variable values are adopted. In other words, a solution to a three-dimensional flux problem satisfying the conditions imposed by a "radiatively independent volume" [*Pinty et al.*, 2004a] has always its equivalent in the one-dimensional representation but at the cost of parameterizing the state variables of the radiation transfer problem in order to ensure the correct balance between the scattered, transmitted, and absorbed radiant fluxes. As a consequence, the two main radiant fluxes available nowadays operationally, i.e., the fractions of scattered and absorbed radiant fluxes, cannot be used together with the retrieved, allometric and presumably true, values of a major state variable, namely, LAI, since this yields an erroneous assessment of the redistribution of energy within the vegetation layer. This problem can, however, be addressed by retrieving the effective state variables, including thus LAI, by inversion of the one-dimensional radiation transfer model to be applied in forward mode in the large-scale models. Such a procedure ensures that simulations of the radiation transfer regimes using prespecified state variables in large-scale models are consistent with the flux values derived from space-borne sensors. Those simulations could thus be further constrained by observations, and meaningful assimilation schemes can be operated.

[7] This paper addresses the issue of the inversion of the two-stream model developed by *Pinty et al.* [2006] against radiant flux values recently available on an operational basis from the Moderate Resolution Imaging Spectroradiometer (MODIS), the Multiangle Imaging Spectroradiometer (MISR) on board the Terra platform and Sea-viewing Wide Field-of-view Sensor (SeaWiFS). The main objective of this contribution is to document the performances of the methodology which is based on inverse theory as promoted in particular by *Tarantola* [1987]. This methodology requires information about the first and second derivatives of the two-stream model. It is noteworthy that this information can be generated in a fully automated manner thanks to the automatic differentiation technique [*Griewank*, 2000]. This leads to a software package allowing the user to perform the inversion of the two-stream model via a numerically and computationally very efficient optimization procedure, while at the same time generating an estimate of the probability density functions (PDFs) for the retrieved variables including thus the effective LAI value. A large series of applications based on model-simulated scenarios are conducted first in order to evaluate the performance of the two-stream inversion/optimization package under controlled conditions. A second set of applications is then performed over midlatitude Earth Observing System (EOS) validation sites using the operational MODIS and MISR surface albedo products. The analysis of the large uncertainties associated with the retrievals promotes the joint use of the SeaWIFS vegetation FAPAR products together with the Terra-estimated surface albedos. We then further derive

Table 1. Mean Values $\mathbf{X}_{\text{prior}}$ and Associated Standard Deviations $\sigma_{\mathbf{X}_{\text{prior}}}$ Used to Set the Diagonal of the a Priori Covariance Matrix $\mathbf{C}_{\mathbf{X}_{\text{prior}}}$[a]

Variable Identification	$\mathbf{X}_{\text{prior}}$	$\sigma_{\mathbf{X}_{\text{prior}}}$
LAI	1.5000	5.0, 10.0, 50.0, and 100.0
$\omega_l(\lambda_1)$	0.1700	0.1200
$d_l(\lambda_1)$	1.0000	0.7000
$r_g(\lambda_1)$[b]	0.1000	0.0959
$\omega_l(\lambda_2)$	0.7000	0.1500
$d_l(\lambda_2)$	2.0000	1.5000
$r_g(\lambda_2)$[b]	0.1800	0.2000

[a] λ_1 and λ_2 correspond to the broadband visible and near-infrared spectral domains, respectively. $\omega_l(\lambda_{1,2})$, $r_g(\lambda_{1,2})$, and $d_l(\lambda_{1,2})$ refer to the single scattering albedo, background albedo, and asymmetry factor, respectively.
[b] With a correlation factor of 0.8862 set in $\mathbf{C}_{\mathbf{X}_{\text{prior}}}$.

PDFs of all the radiant fluxes that can be simulated via the two-stream model, in particular, those radiant fluxes not belonging to the measurement set, for example, the fraction of flux absorbed by the ground underneath the vegetation layer in the solar domain.

2. Outline of the Inversion Methodology

2.1. The Two-Stream Forward Model

[8] Since large-scale models will likely continue operating one-dimensional models to represent surface processes for the foreseeable future, *Pinty et al.* [2006] have revisited and updated the two-stream formulations proposed by *Meador and Weaver* [1980], *Dickinson* [1983], *Dickinson et al.* [1986], and *Sellers* [1985]. The study of *Pinty et al.* [2006] was conducted with the aim to improve the accuracy and correctness of existing solutions provided for (1) the single scattering regime in the canopy, (2) the multiple scattering regime under high scattering conditions such as those associated with a snow-covered background, and (3) three-dimensional effects induced by unresolved internal variability in the vegetation layer. In addition, these improvements were proposed in a frame that should facilitate the coupling of the radiation transfer processes between the surface and the atmospheric layers; for example, the two-stream solutions to the surface problem are given in the same analytical form as those already derived by *Meador and Weaver* [1980] for the atmosphere. For all practical purposes, this should logically translate into a somewhat reduced cost of software implementation while preserving current maintenance efforts.

[9] In summary, the proposed radiation transfer solution for simulating the scattered, transmitted, and absorbed radiant fluxes over land surfaces is generated by the sum of three separate contributions, namely, (1) the black background (no scattering from the background), the solution of which follows exactly the one from the study of *Meador and Weaver* [1980], (2) the black canopy (no scattering by canopy elements), essentially associated with the vegetation structure, and (3) the remaining contribution involving multiple scattering events between the canopy and the background approximated by the same solution of *Meador and Weaver* [1980] except in the case of an external isotropic source of illumination. Each of the three separate contributions involves the use of effective variables whenever the unresolved variability of the leaf area density becomes significant, i.e., deviation from the homogeneous one-dimensional plane-parallel problem. Those effective variables are the leaf reflectance r_l and transmittance t_l, or alternatively the leaf single scattering albedo $\omega_l = r_l + t_l$ and the ratio $d_l = r_l/t_l$ (identified here as the asymmetry factor) and the LAI. Solutions to the problem satisfying the specific cases involving preferred leaf orientation are given separately [see *Pinty et al.*, 2006, Appendix A]. The associated boundary conditions are the downward radiant flux density from the atmosphere specified as a function of the fraction of direct (collimated) and diffuse (assumed isotropic) radiation and the upward radiant flux at the bottom of the vegetation layer specified via the true (and not effective) albedo of the background.

[10] The spectrally invariant effective LAI and the spectrally dependent effective scattering properties are derived in a meaningful manner as explained in the work of *Pinty et al.* [2004a, section 3.3.2] and *Pinty et al.* [2006, section 2.3]. Their domain-averaged values are indeed forced to satisfy the one-dimensional turbid medium representation of the three radiant fluxes taken together irrespective of the three-dimensional internal variability of the geophysical systems. Accordingly, the effective LAI is obtained from the analysis of the true radiant flux directly transmitted along direction μ_0 (cosine of the Sun zenith angle) to the background level z_{bgd}, i.e., $\text{LAI} = -2.0\mu_0 \log[T^{\downarrow}_{\text{Black canopy}}(z_{\text{bgd}}, \mu_0)]$, while the estimate of the leaf reflectance r_l and leaf transmittance t_l effective values is achieved so that they enable matching the joint reflected and diffusely transmitted radiant fluxes corresponding to the black background contribution in each spectral domain of relevance. The dependency of these effective spectrally invariant (variant) values with respect to the Sun zenith angle was found weak enough to be parameterized in simple terms [*Pinty et al.*, 2006, equation (4)] (neglected [*Pinty et al.,* 2004a, section 3.3.2]).

2.2. The Inversion Methodology

[11] In all generality, the formulation of an inverse problem aims at optimizing the use of available information specified through a priori knowledge on the values of the model parameters $\mathbf{X}$ (those listed in Table 1), the measurements $\mathbf{d}$ (corresponding to the radiant fluxes simulated by the model), and the constraint provided by the two-stream radiation transfer model $M(\mathbf{X})$. Such a formulation is relatively generic for solving ill-posed problems. The following outline is given here for the sake of completeness, although it is quite common to various applications in geosciences [see, e.g., *Tarantola and Valette*, 1982; *Enting et al.*, 1995; *Kaminski et al.*, 1999; *Lavergne et al.*, 2007].

[12] The associated algebra is particularly convenient [see *Tarantola*, 1987] if the measurements and the a priori knowledge on the model parameters can be approximated by Gaussian probability distributions, i.e., if they can be both represented by their mean values $\mathbf{d}$ and $\mathbf{X}_{\text{prior}}$ and associated covariance matrices denoted by $\mathbf{C}_{\mathbf{d}}$ and $\mathbf{C}_{\mathbf{X}_{\text{prior}}}$, respectively. If, in addition, the local linearization provides a good approximation for the nonlinear model $M(\mathbf{X})$, then the a posteriori probability distribution $P(\mathbf{X})$ is close to Gaussian as well. Hence $P(\mathbf{X})$ can be approximated by its mean value and covariance matrix denoted $\mathbf{X}_{\text{post}}$ and $\mathbf{C}_{\mathbf{X}_{\text{post}}}$, respectively

(where ^{T} represents the transpose operator and $\mathbf{C}^{-1}$ the inverse matrix of $\mathbf{C}$):

$$P(\mathbf{X}) \approx \exp\left(-\frac{1}{2}(\mathbf{X}-\mathbf{X}_{\text{post}})^{\mathrm{T}}\mathbf{C}_{\mathbf{X}_{\text{post}}}^{-1}(\mathbf{X}-\mathbf{X}_{\text{post}})\right) \quad (1)$$

$\mathbf{X}_{\text{post}}$ represents the maximum likelihood estimator of the mean of $P(\mathbf{X})$ and minimizes the cost function $J(\mathbf{X})$ expressed as follows:

$$J(\mathbf{X}) = \frac{1}{2}\Big[(M(\mathbf{X})-\mathbf{d})^{\mathrm{T}}\mathbf{C}_{\mathbf{d}}^{-1}(M(\mathbf{X})-\mathbf{d}) + (\mathbf{X}-\mathbf{X}_{\text{prior}})^{\mathrm{T}}\mathbf{C}_{\mathbf{X}_{\text{prior}}}^{-1}(\mathbf{X}-\mathbf{X}_{\text{prior}})\Big] \quad (2)$$

[13] The first term on the right-hand side of equation (2) quantifies the mismatch between the model simulations and the measurements, while the second term expresses the constraint given by a priori knowledge on the model parameters. The covariance matrices expressing the uncertainties in the measurements and in the a priori knowledge on model parameters can be conceived of as weighting factors in equation (2). If the covariance matrices are diagonal (implying zero correlation between the elements), then equation (2) reduces to a least squares formulation, and each component of $\mathbf{d}$ and $\mathbf{X}_{\text{prior}}$ is weighted in inverse proportion to the uncertainty level that is associated with it; that is, a poor knowledge about a given model parameter is specified by a corresponding large variance value and thus carries low weight. As stated previously, the use of a priori information on the parameters enables transforming an ill-posed into a well-posed problem. Parameter values that deviate much from the a priori value, in terms of a priori uncertainty, are associated (penalized) with a high value of the cost function and are thus unlikely to occur. Note that the formulation of equation (2) is rather generic and can be adopted for inversion purposes at a single time of observation and for a series of inversions coupled in the temporal domain.

[14] The inverse problem is solved with a gradient algorithm minimizing equation (2) which iteratively evaluates both $J(\mathbf{X})$ and its gradient $\nabla J(\mathbf{X})$ with respect to $\mathbf{X}$. The exact evaluation of this gradient can be achieved via the adjoint model of J which also saves significant computer time by contrast to finite difference techniques [*Giering and Kaminski*, 1998]. An additional term, which drastically increases the cost function in case of unrealistic combinations of model parameters [not shown but entering equation (2)], essentially excludes the corresponding regions in the model parameter space. Imposing the model parameter values to be restricted within the domain of their physical meaning, for instance, LAI ≥ 0, is indeed a way of adding soft bounds on the parameter space.

[15] Under the regularity conditions mentioned above, the Hessian $\nabla^2 J(\mathbf{X}_{\text{post}})$ at the minimum of J approximates the inverse of the a posteriori covariance matrix $\mathbf{C}_{\mathbf{X}_{\text{post}}}$. Comparison with the a priori uncertainty indicates how well individual directions in the space of model parameters are observed through the measurements. Eigenvectors of $\mathbf{C}_{\mathbf{X}_{\text{post}}}$ indicate the directions in the parameter space that are independently resolved by the observations, and the corresponding eigenvalues quantify the uncertainties associated with the retrievals. Comparison of the values in the a priori and a posteriori covariance matrices thus expresses, in quantitative terms, the knowledge gain from the inversion procedure, i.e., from using actual measurements, together with their associated uncertainties and the model $M(\mathbf{X})$.

[16] The generation of the a posteriori covariance matrix can be exploited further to evaluate the PDFs of quantities $(\mathbf{X})$ simulated by the model [see *Kaminski et al.*, 2003; *Rayner et al.*, 2005]. In our case, the quantities of interest are the radiant fluxes, in particular, those that are not part of the measurement set, for example, the flux transmitted through the vegetation canopy layer for a remote-sensing application. Once the inversion has been performed, the uncertainty on the radiant fluxes, including thus those that are unknown or poorly known, can be expressed by the covariance matrix $\mathbf{C}_{\text{post}}^{\text{Flux}}$:

$$\mathbf{C}_{\text{post}}^{\text{Flux}} = \mathbf{G}\mathbf{C}_{X_{\text{post}}}\mathbf{G}^{\mathrm{T}} \quad (3)$$

where $\mathbf{G}$ denotes the Jacobian matrix of $M(\mathbf{X})$ at minimum, i.e., $\mathbf{G} = \partial M(\mathbf{X}_{\text{post}})/\partial \mathbf{X}$ with a linearization around the mean values $\mathbf{X}_{\text{post}}$. This matrix quantifies the correlation between the posterior uncertainties of the fluxes and notably those incorporated in the measurement set. It allows us to approximate the posterior PDFs of the fluxes of interest.

[17] In the present two-stream model applications, the software code calculating the first and second derivatives has been generated automatically by the compiler tool Transformation of Algorithms in C++ (TAC++) [*Giering and Kaminski*, 1998] available from FastOpt (http://www.FastOpt.com/). The software routines for achieving minimization (dfpmin) and matrix inversion [performed by computing the eigenvalues and eigenvectors of this matrix (jacobi)] are provided by the scientific library available from *Press et al.* [1986].

3. Performances of the Inversion Procedure

[18] In order to assess the accuracy of the retrievals from the inversion package, a series of four different Gaussian distributions of LAI were defined around a constant mean LAI value such as to span very sparse and dense canopy conditions. This was realized by increasing progressively $\sigma_{\mathbf{X}\text{prior}}(\text{LAI})$ from 5.0 to 10.0, 50.0, and finally 100.0 around a constant mean LAI value of 1.50. Every LAI value randomly selected within each of these four distributions was then combined with the remaining model parameter values, themselves also selected at random from their respective prior PDFs as indicated in Table 1. Note that $\mathbf{C}_{\mathbf{X}\text{prior}}$ is not strictly diagonal but incorporates a correlation between the soil albedo values in the broadband visible and near-infrared range [see, e.g., *Price*, 1995]. The correlation value between $r_g(\lambda_1)$ and $r_g(\lambda_2)$ was set at 0.8862 and specifies additional constraints on the retrievals.

[19] This ensemble of 2000 [4 values of $\sigma_{\mathbf{X}\text{prior}}(\text{LAI}) \times$ 500 samples of spectrally variant model parameter values] vegetation scenarios thus includes conditions that are all belonging to the set of possible realizations (specified via their prior PDFs) while recognizing the large natural variability in a key state variable, namely, the LAI. This data set allows us to assess the deviations between the true and the a posteriori model parameter values under a large variety of

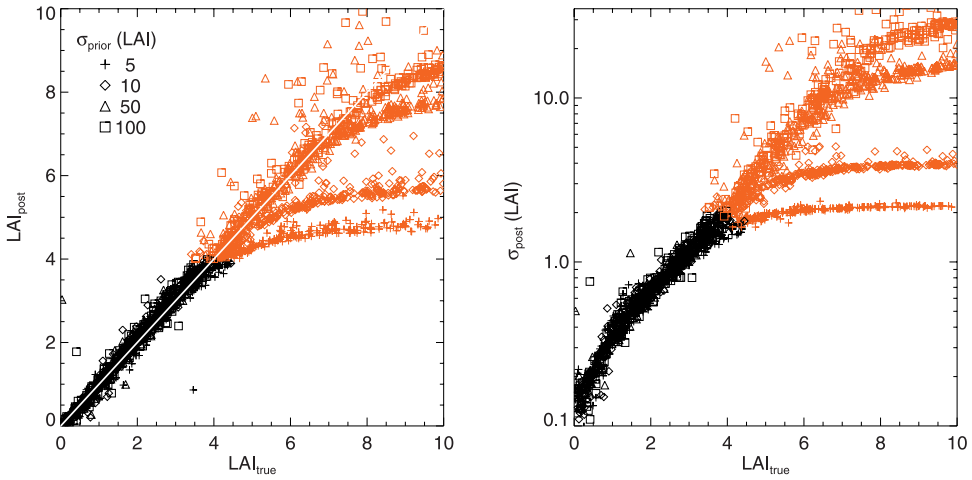

Figure 1. Left panel: relationship between the true and the retrieved LAI values. Right panel: values estimated for $\sigma_{\mathbf{X}\text{post}}$(LAI), extracted from the diagonal of the a posteriori covariance matrix. Different symbols are used to isolate results from cases corresponding to each of the four selected $\sigma_{\mathbf{X}\text{prior}}$(LAI) values. In addition, a red color code is adopted to identify those retrievals where LAI takes values higher than 4.0, i.e., vegetation approaching the semi-infinite situation.

instances, including those featuring a radiatively semi-infinite vegetation canopy, i.e., implying thus a negligible/indiscernible impact of the background albedo on the fluxes scattered upward by the canopy [see, e.g., *Gobron et al.*, 1997].

[20] The radiant flux values were estimated in the two broadband visible (identified with subscript 1) and near-infrared (identified with subscript 2) domains of interest, respectively, using the two-stream model developed by *Pinty et al.* [2006], for each individual scenario. The bi-hemispherical flux values generated for each of these individual scenarios were then used as a measurement set in the inversion package, and the retrievals from various combinations of such synthetic measurements were analyzed. The inversion package was operated for a set of measurement configurations including the scattered flux in the two broadband spectral domains (noted R_1 and R_2) together with the absorbed flux in the visible domain (noted A_1). This configuration, labeled $R_1R_2A_1$, acknowledges the availability of global surface albedo and vegetation FAPAR products from various sources.

[21] The covariance matrix associated with these synthetic measurements, $\mathbf{C}_d$, is assumed diagonal, and the baseline setup is made with standard deviation values of 0.1 for the fraction of absorbed flux A_1 and 5% of their estimated values for the fraction of measured reflected R_1 and R_2 spectral fluxes. These values are selected on the basis of information involving product intercomparison exercises [see, e.g., *Jin et al.*, 1999; *Pinty et al.*, 2004b] as well as product comparison against ground-based estimates [see, e.g., *Turner et al.*, 2004; *Gobron et al.*, 2006].

[22] Each of these 2000 inversion runs required 8.0×10^{-3} s on average, although the package has not yet been optimized for efficiency. These small numbers correspond to the user time (defined here as the total number of CPU seconds that the process spends in user mode) on a PC (Xeon 2.4 GHz) with 2 GB RAM, running under the Linux 2.6 kernel. The software was compiled using the gcc-4.0.1 compiler with no optimization flag.

3.1. Accuracy of the Retrievals

[23] The retrievals of LAI are displayed in Figure 1. The left panel exhibits the relationship between the true and the retrieved LAI values, and the right panel shows the corresponding values of $\sigma_{\mathbf{X}\text{post}}(LAI)$ (with logarithmic scale), extracted from the a posteriori covariance matrix. Different symbols are used to isolate results from conditions corresponding to each of the four selected $\sigma_{\mathbf{X}\text{prior}}(LAI)$ values. In addition, a red color code is adopted to identify those retrievals where the retrieved LAI takes values larger than 4, i.e., vegetation approaching or matching the radiatively semi-infinite condition.

[24] The agreement between the series of true LAI values and those retrieved by inversion is remarkable, and the associated uncertainties remain within a quite reduced range [$\sigma_{\mathbf{X}\text{post}}$(LAI) $\approx 0.35 \times$ LAI$_{\text{post}}$] for all canopy conditions where the optimized LAI values are less than 4. In all these cases, the estimated uncertainty $\sigma_{\mathbf{X}\text{post}}$(LAI) is much lower than its a priori value for each of the four selected $\sigma_{\mathbf{X}\text{prior}}$(LAI) values indicated in the left panel in Figure 1. For the very few instances where the quality of the retrievals deteriorates, the cost function $J(\mathbf{X})$ returns values located on the right-hand side of its histogram. Figure 1 also exposes the dependency of the retrieved PDFs for LAI with respect to the specified value of the a priori uncertainty for canopy conditions approaching the semi-infinite conditions. For such conditions, the deviation between the retrieved and true values of LAI is getting large, and this situation can be compensated only (all inputs remaining the same) by increasing the a priori uncertainty in the covariance matrix on this particular model parameter. The right panel shows that an uncertainty value $\sigma_{\mathbf{X}\text{prior}}$(LAI) of 5.0 induces a saturation of both the retrieved LAI and $\sigma_{\mathbf{X}\text{post}}$(LAI). Accordingly, the PDFs of the LAI retrieved under such conditions may not cover the possible range of LAI values. By contrast, the progressive increase in the $\sigma_{\mathbf{X}\text{prior}}$(LAI)

values, from 5.0 to 10, 50, and 100.0, translates into an improved accuracy in the mean LAI values, yielding unbiased estimates over a larger range of LAI, associated with increasing (with significantly fewer occurrences of saturation) values of their uncertainty. In other words, for conditions where LAI is larger than 4, the inversion package still delivers unbiased mean estimates but associated with wider distributions (PDFs). It is noteworthy that the use of too large $\sigma_{\mathbf{X}_{\text{prior}}}$(LAI) (according to the expected range in LAI for realistic biophysical scenarios) yields extremely large $\sigma_{\mathbf{X}_{\text{post}}}$(LAI) values indicating thus that there is no knowledge gain by performing the inversion.

[25] Results from Figure 1 indicate the limited dependency of the LAI optimization procedure with respect to the a priori information about the expected mean values. In the specific case of dense vegetation canopies, the physics of radiation transfer processes and the performances of spaceborne sensors operating in the solar domain are such that any accurate and precise estimate of LAI values is an extremely challenging task: retrieving accurate (large) LAI values associated with limited uncertainty [small $\sigma_{\mathbf{X}_{\text{post}}}$(LAI) values]. Under such geophysical situations, the inversion returns a posteriori covariance matrices that are mostly determined by the information specified in the a priori knowledge. As a matter of fact, the interpretation of remote-sensing flux products hardly translates into improving our current knowledge on the geophysical system.

[26] This state of affairs is confirmed by assessing the quality of the retrievals with respect to the spectrally dependent model parameters. To this end, Figures 2 and 3 report on the relationships between the true and the retrieved mean parameter values (left panels) as well as the uncertainty (right panels) associated with these retrievals, i.e., the values of $\sigma_{\mathbf{X}_{\text{post}}}$, in the broadband visible and near-infrared domains, respectively. For those geophysical scenarios matching the semi-infinite conditions (red colored symbols), the single scattering albedos are quite accurately retrieved in both spectral bands since this is the only significant state variable of interest for the physical problem to be solved. This situation translates into unbiased estimates of $\omega_l(\lambda_{1,2})$ (top left panels) associated with small uncertainty values (top right panels).

[27] By contrast, and as expected, retrievals of background albedos (middle panels) performed under those semi-infinite canopy conditions correspond to the a priori knowledge on both the mean and the uncertainty values. There is no gain in knowledge on these model parameters in relation with the available measurements, and the inversion package thus behaves reliably. For geophysical conditions designed with low and medium LAI values, the quality of the retrievals of both $\omega_l(\lambda_{1,2})$ and $r_g(\lambda_{1,2})$ is fluctuating almost independently from $\sigma_{\mathbf{X}_{\text{prior}}}$ values. Note that the $\sigma_{\mathbf{X}_{\text{post}}}$ value for $\omega_l(\lambda_{1,2})$ and $r_g(\lambda_{1,2})$ may, in some geophysical instances, and because of the nonlinearity of the two-stream model, even exceed its a priori value. A detailed documentation and discussion of the behavior of the inversion procedure in these few instances are given in the work of *Lavergne et al.* [2006].

[28] The accurate estimation of the predominant scattering regime (bottom panels) is very difficult in both spectral domains. Indeed, the inversion package returns PDFs of $d_l(\lambda_{1,2})$ which are about the same as those corresponding to the a priori. The most favorable conditions for reducing uncertainty on this model parameter must include those offering a discernible signature of the downward scattered transmitted flux [see *Pinty et al.*, 2004a, section 3.3.2].

3.2. Examples of Covariance Matrices

[29] The interpretation of these results also greatly benefits from the availability of the full a posteriori covariance matrices. Figure 4 displays the corresponding correlation matrices for different measurement configurations, estimated in the case of a green leaf vegetation canopy made up with LAI of 1.75 overlying a medium brightness soil condition; that is, $r_g(\lambda_1)$ and $r_g(\lambda_2)$ are set at 0.12 and 0.21, respectively. The top left panel is a reminder of the correlations corresponding to the a priori covariance matrix. Accordingly, the background albedo in the two spectral domains, namely, $r_g(\lambda_1)$ and $r_g(\lambda_2)$, shows a positive (blue tone) correlation value (see section 3). The knowledge of the absorbed flux in the visible domain (labeled A_1, top right panel) induces a strong positive correlation between the leaf single scattering albedo in this same spectral domain and the LAI, together with slightly negative correlations with the background albedos. These patterns express the coupling between the optical thickness of the layer, LAI, and its lower boundary condition, when single scattering regime dominates; for example, interception of radiation is the main driver of the radiation transfer process. Note that the direction of the coupling between the model process parameters is indicated by the sign of the correlation; that is, a negative correlation between the uncertainty in two parameters means that underestimating the first has the same effect as overestimating the second.

[30] The addition of the upward scattered flux in the two spectral domains in the set of measurements, configuration labeled $R_1R_2A_1$ (bottom left panel), renders the shape of the a posteriori correlation matrix somewhat more complex: A positive correlation is observed in the spectral dimension between the two leaf single scattering albedo values. The observed negative correlations between the single scattering albedo and the background albedo in both spectral domains are a consequence of the balance between the scattering contribution involving the leaf canopy only, i.e., the black background, as opposed to the one involving the lower boundary condition, i.e., mainly the black canopy. Incidentally, one can also notice the positive correlation occurring in the visible domain between the leaf single scattering albedo $\omega_l(\lambda_1)$ and the asymmetry factor $d_l(\lambda_1)$; indeed, a decrease in the leaf scattering efficiency must be compensated by an increase in the backward scattering regime, hence larger values of $d_l(\lambda_1)$, in order to maintain the balance between the absorbed and scattered fluxes by the canopy.

[31] The inclusion of the transmitted fluxes in the measurement configuration $R_1R_2A_1A_2T_1T_2$ (bottom right panel) translates notably into a negative correlation between the leaf asymmetry factor d_l in both spectral domains and LAI. The latter shows that an increase in LAI can indeed be partly compensated by an enhancement in the efficiency of forward scattering regime (for example, if the canopy layer becomes optically thicker, the leaves have to transmit more radiation, while the leaf single scattering albedo has to increase).

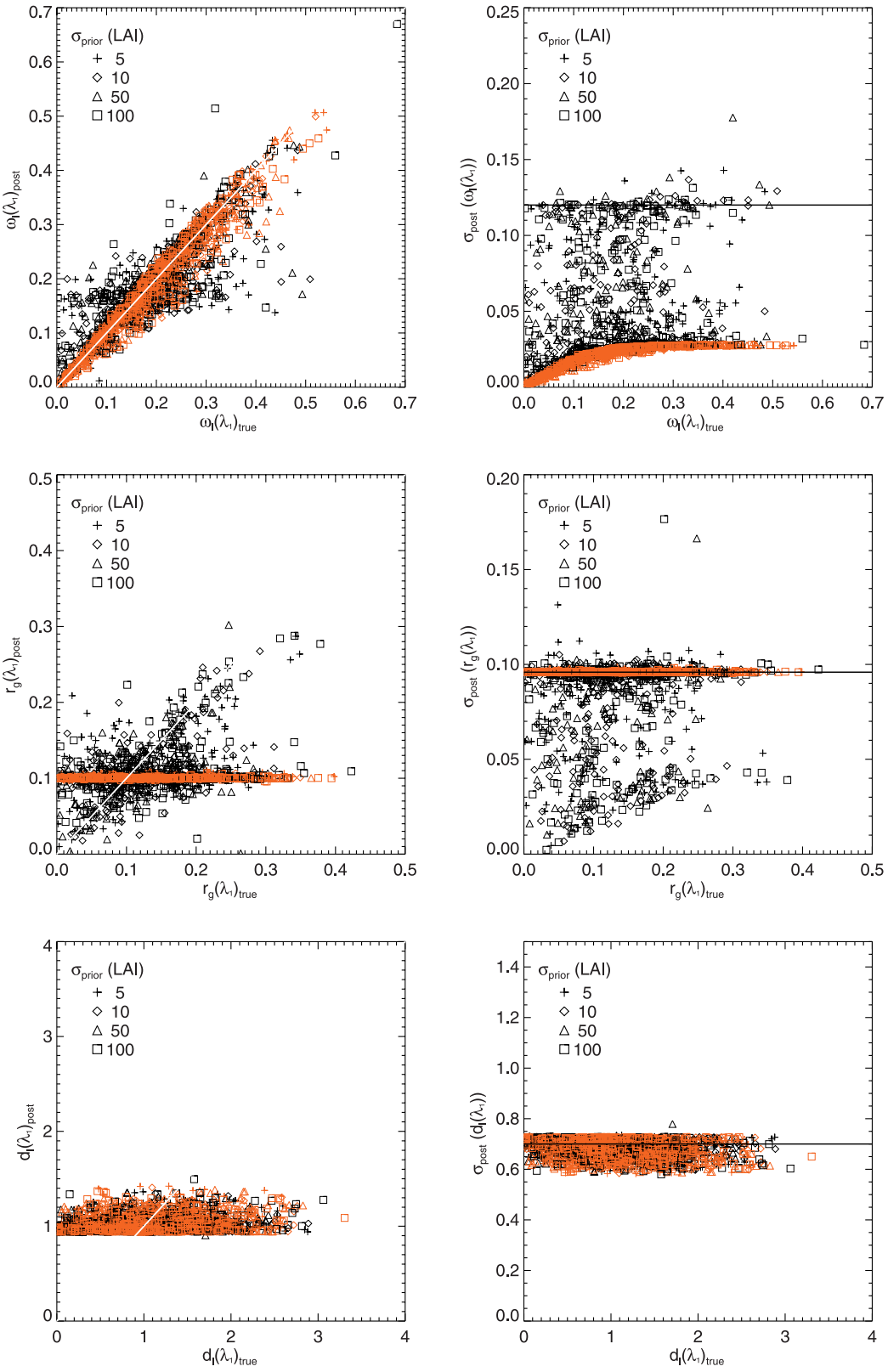

Figure 2. Left panels display the relationships between the true and the mean a posteriori model spectral parameter values in the broadband visible domain. $\omega_l(\lambda_1)$, $r_g(\lambda_1)$, and $d_l(\lambda_1)$ correspond to the single scattering albedo, background albedo, and asymmetry factor, respectively. Right panels show the $\sigma_{\mathbf{X}\text{prior}}$ (horizontal lines) and $\sigma_{\mathbf{X}\text{post}}$ values [different symbols are used to isolate results from cases corresponding to each of the four selected $\sigma_{\mathbf{X}\text{prior}}$(LAI) values]. The red color code identifies those retrievals where LAI takes values higher than 4.0, i.e., vegetation approaching the semi-infinite situation.

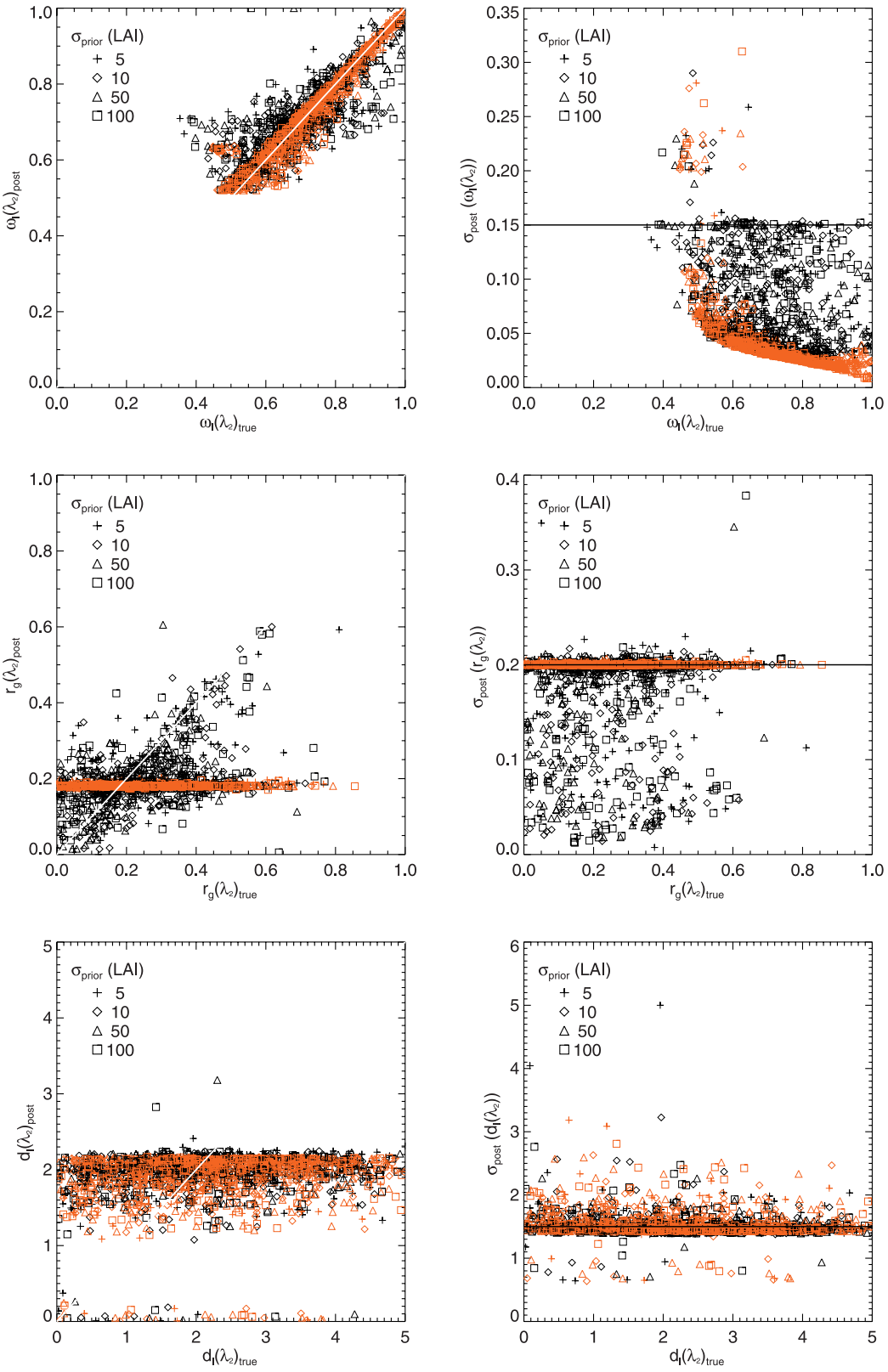

Figure 3. Same as Figure 2, except for the case of the model spectral parameter values in the broadband near-infrared domain, i.e., $\omega_l(\lambda_2)$, $r_g(\lambda_2)$, and $d_l(\lambda_2)$.

[32] The above examples of a posteriori correlation matrices expose the information content delivered by the two-stream inversion package. These covariance matrices display the multiple constraints that must be satisfied when optimizing equation (2) for the given measurement configuration. Since these constraints follow the physical processes embedded into the two-stream model, the analysis of these matrices is quite relevant for learning about the model

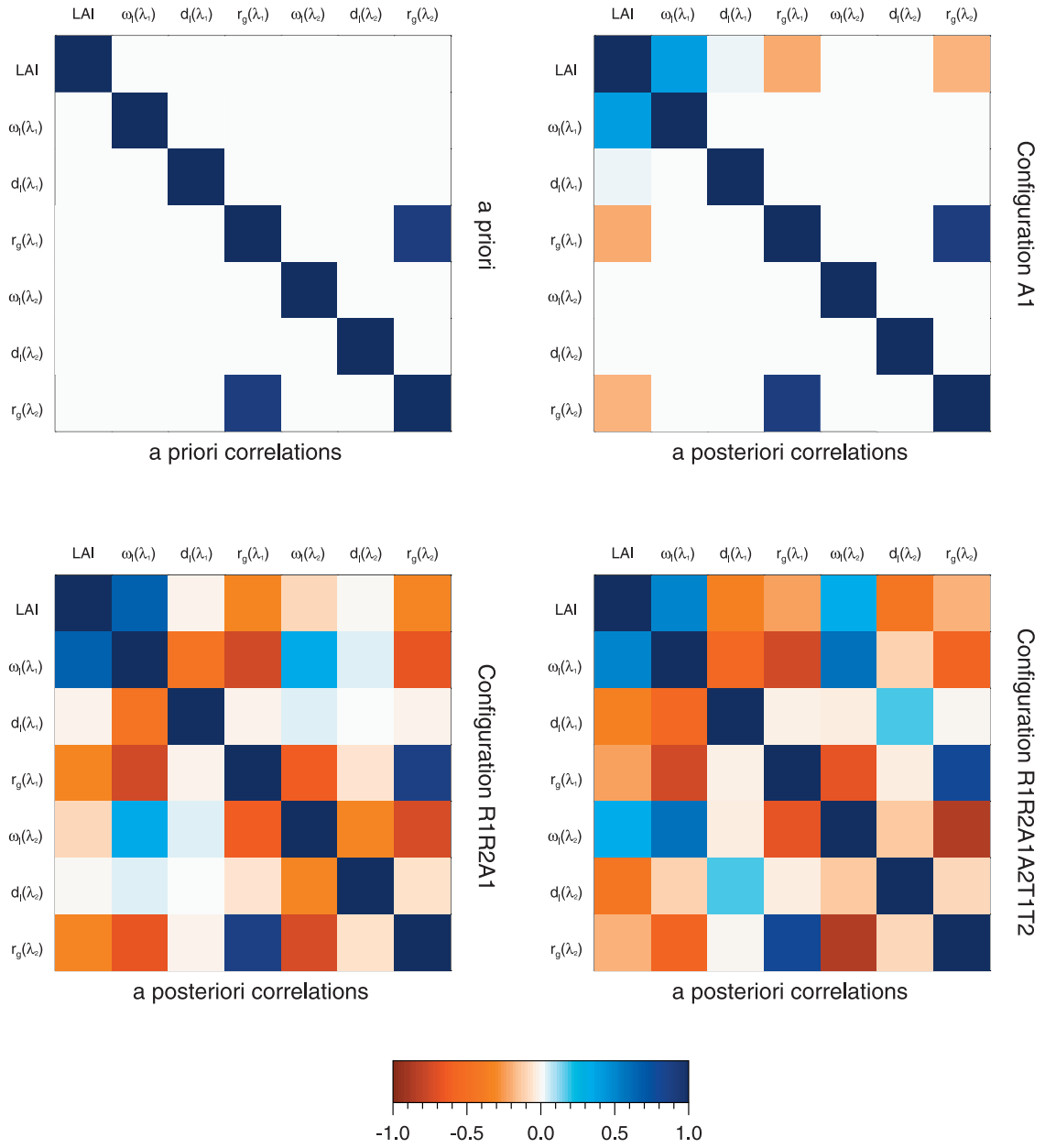

Figure 4. Correlations between model parameter extracted from the a posteriori covariance matrices estimated in the case of a green leaf vegetation canopy made up of a LAI of 1.75 overlying a medium brightness soil condition, i.e., $r_g(\lambda_1)$ and $r_g(\lambda_2)$ are set at 0.12 and 0.21, respectively. Positive (negative) correlations are featured by blue (red) color tones.

behavior. Additional examples of such covariance matrices, discussed in the work of *Lavergne et al.* [2006], have been produced in the frame of the current model-based series of inversion exercises.

4. Application Examples Using Terra Albedo Products

[33] Measurements from the MODIS and MISR sensors on board the Terra platform are analyzed by operational algorithms in order to generate surface albedo products. As a matter of fact, these products differ in many respects regarding notably the way they handle the contributions because of the field of downward diffuse intensities [see, e.g., *Pinty et al.*, 2005]. For instance, the MODIS sensor delivers, every 16-day period, bi-hemispherical reflectance (BHR) values (associated with an incident intensity field which is purely isotropic) that are intrinsic surface properties (this product is called "white sky" albedo [*Schaaf et al.*, 2002], and only those delivered with good confidence levels [Quality Assessment flag values of 0 and 1] are considered here). The retrieval algorithm selected for the processing of data acquired by MISR generates BHRs as well but for the particular Sun illumination and atmospheric conditions at the time of the satellite measurement only [*Martonchik et al.*, 1998]. Since the MISR products include information about

Table 2. Identification and Main Characteristics of the Selected Sites

Field Site Identification	Geographical Coordinates	Vegetation Type	Expected Radiation Transfer Regime[a]
Dahra[b] (Senegal)	15°22′N	Semi-arid grass	"Fast"
	15°26′W	Savannah	Short and homogeneous over 1–2 km
Agro[c] (United States)	40°0′N	Broadleaf crops including	"Slow"
	88°17′W	Corn and soybean	Mixed vegetation with different land cover type
Konza[c] (United States)	39°4′N	Grassland, shrubland, and cropland	"Slow"
	96°33′W		Mixed vegetation with different land cover type
Mongu[d] (Zambia)	15°26′S	Mixed shrubland and woodland	"Resonant"
	23°15′E		Intermediate height but low density vegetation

[a]Based on the studies of *Davis and Marshak* [2004] and *Gobron et al.* [2006].
[b]See *Fensholt et al.*, 2004.
[c]See *Turner et al.*, 2004.
[d]See *Huemmrich et al.*, 2005.

the intrinsic surface anisotropy, i.e., the so-called modified Rahman-Pinty-Verstraete model parameters [*Engelsen et al.*, 1996], it becomes possible to generate BHR values analogous to the MODIS white sky albedos. In addition, selected spectral conversion formulae [see *Liang et al.*, 1999; *Liang*, 2000; *Govaerts et al.*, 2006] were adopted in order to derive comparable broadband visible and near-infrared products from both sensors (see *Pinty et al.* [2004b] for comparison of results). An aggregation over each 8-day period of the year has been performed on these MISR products in order to maximize their geographical coverage. It must be emphasized here that MODIS and MISR albedo products are generated from algorithms solving an atmospheric radiation transfer problem with respect to its lower boundary condition, with no specific assumption on the surface land cover type and condition.

[34] In the context of the present series of applications, time series of remote-sensing products estimated during year 2001 over specific midlatitude sites associated with field activities have been selected (see Table 2). This selection encompasses contrasted biome type and vegetation phenological cycles so that our inverse procedure can

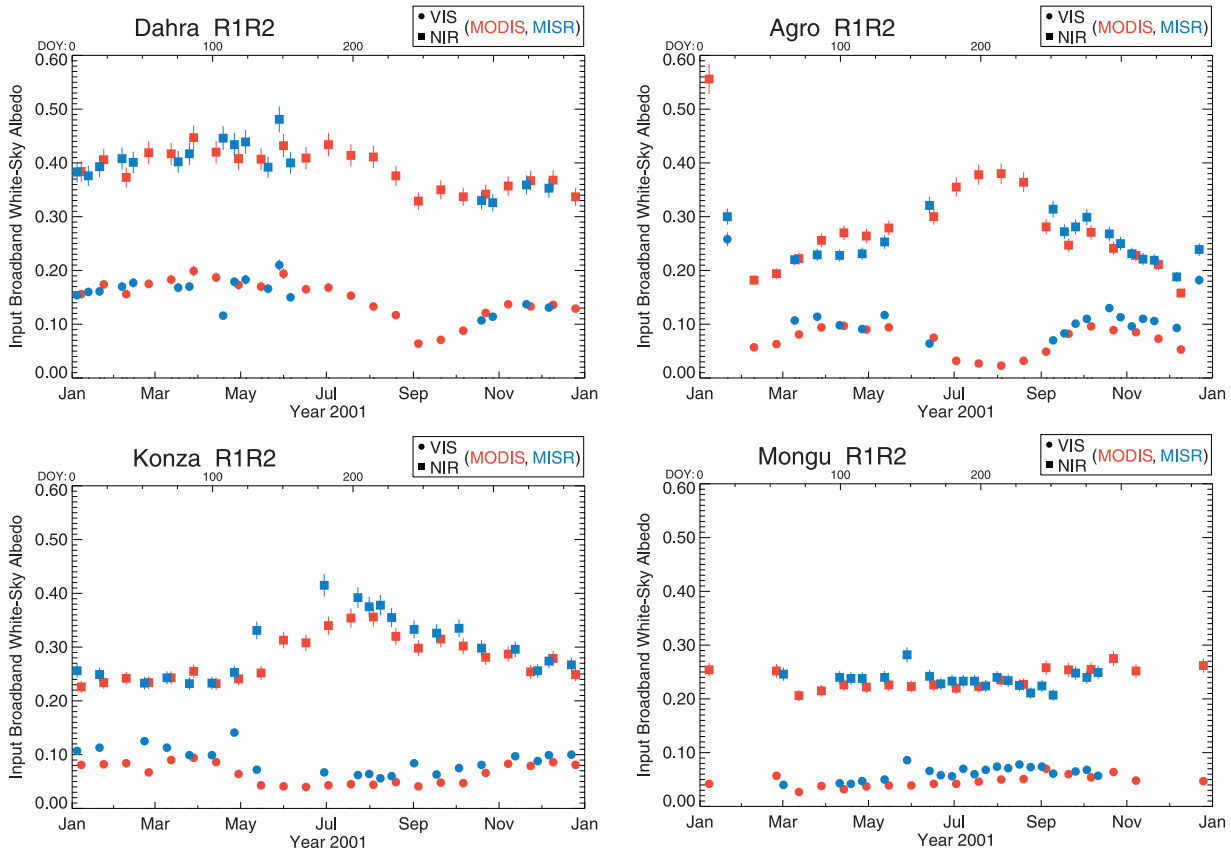

Figure 5. Time series of the broadband visible (full circle symbols) and near-infrared (squared symbols) MODIS (red color) and MISR (blue color) BHR-white sky albedo products over the site of Dahra (top left panel), Agro (top right panel), Konza (bottom left panel), and Mongu (bottom right panel), respectively. A short description of the sites is provided in Table 2. MODIS (MISR) values are plotted on day 8 (4) of every 16-day (8-day) period.

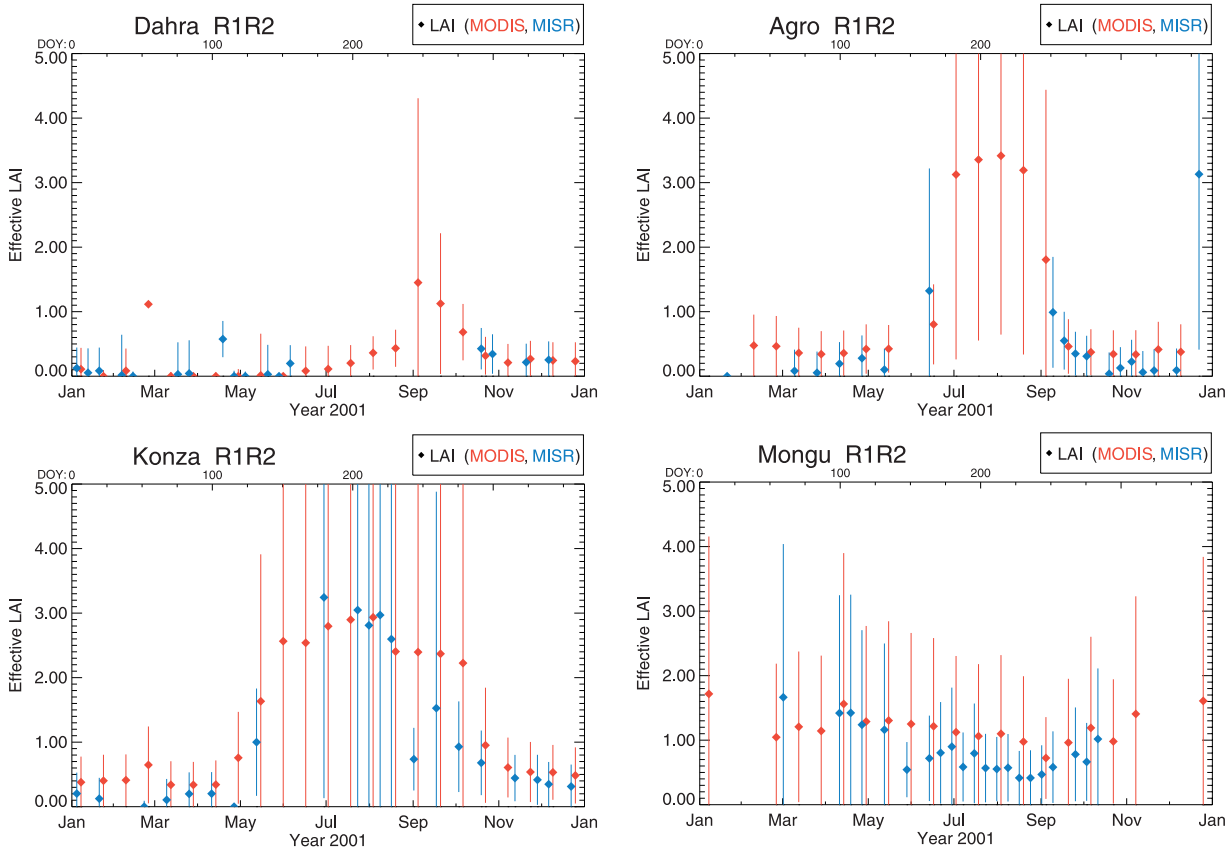

Figure 6. Time series of the effective leaf area index (LAI) retrieved from the MODIS (red color) and MISR (blue color) BHR-white sky albedo products over the site of Dahra (top left panel), Agro (top right panel), Konza (bottom left panel), and Mongu (bottom right panel), respectively. A short description of the sites is provided in Table 2. MODIS (MISR) values are plotted on day 8 (4) of every 16-day (8-day) period. The associated uncertainty values, i.e., the standard deviation $\pm\sigma_{\mathbf{x}_{\text{post}}}(\text{LAI})$, returned by the inversion package on the diagonal of the a posteriori covariance matrix are reported with vertical bars.

be evaluated under different environmental conditions. In addition, each of these sites samples a different radiation transfer regime associated with the three-dimensional internal but unresolved variability of the leaf area density (see *Gobron et al.* [2006] for detailed discussions). Figure 5 displays the evolution of the broadband visible and near-infrared MODIS and MISR BHR-white sky albedo products over the four selected sites. On this figure, the MODIS values are plotted on day 8 of every 16-day period, while the MISR values are associated with day 4 of every 8-day period. The overall good agreement between the two sets of products is noticeable given the major differences in the input data sets and in the scientific strategies devised for these surface albedo retrieval algorithms. Note, however, that these differences may exceed the a priori uncertainty (5% of their estimated values) assigned in the measurement covariance matrix $\mathbf{C}_{\text{d}}$. The intra-annual variations in BHR values over the four selected sites show different types of situations: (1) high BHR values in both spectral domains with in-phase changes in August and September months over Dahra, (2) low (high) BHR values in the visible (near-infrared) with well-pronounced antiphase variations over Agro between June and September, (3) low (high) BHR values in the visible (near-infrared) with relatively limited antiphase variations over Konza, and (4) low BHR values in both spectral domains with no strong seasonal variations over Mongu. This variety of situations thus yields a challenging set of conditions for the inversion package given that information gathered in situ report the occurrence of changes in vegetation cover and density during the course of year for all four sites.

[35] The values assigned to the model parameter in the a priori covariance matrix $\mathbf{C}_{\mathbf{x}_{\text{prior}}}$ are the same as in Table 1 with $\sigma_{\mathbf{x}_{\text{prior}}}(\text{LAI}) = 5.0$. In the following sections, retrieval results with a measurement configuration including the two broadband spectral albedos only (labeled as R_1R_2 on the figures) from the Terra platform will be discussed. All results reported in this paper were produced in static mode that is, with no updating of the a priori knowledge (on the model parameters and the associated covariance matrix), based on retrievals performed at previous time steps.

4.1. The Spectrally Invariant Effective Leaf Area Index

[36] The retrieved effective LAI values and their associated uncertainty level, $\pm\sigma_{\mathbf{x}_{\text{post}}}(\text{LAI})$, are shown in Figure 6 for each of the four sites. Besides the expected seasonal trends which are apparent on each panel, one may notice first the occurrence of large uncertainties when LAI takes

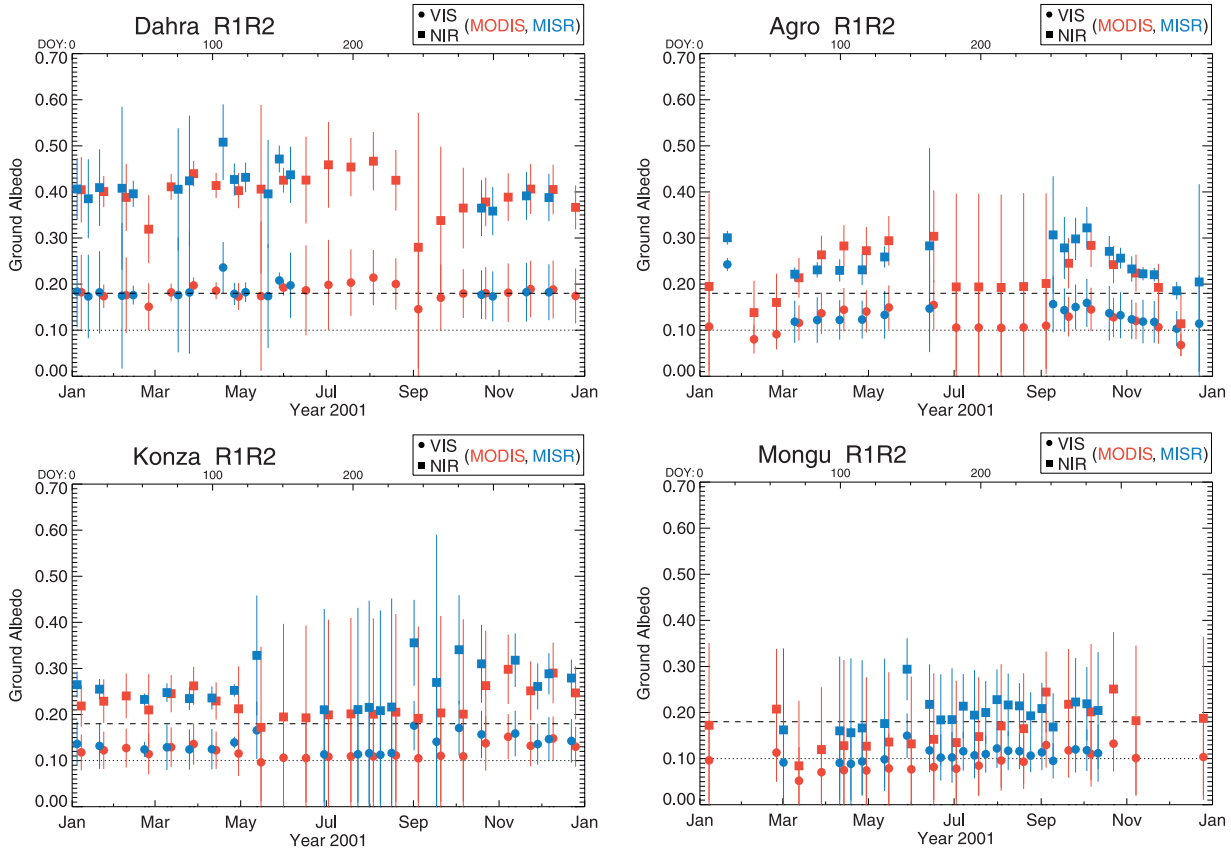

Figure 7. Time series of the retrieved true background albedo from the broadband visible (full circle symbols) and near-infrared (squared symbols) MODIS (red color) and MISR (blue color) BHR-white sky albedo products over the site of Dahra (top left panel), Agro (top right panel), Konza (bottom left panel), and Mongu (bottom right panel), respectively. MODIS (MISR) values are plotted on day 8 (4) of every 16-day (8-day) period. The associated uncertainty values, i.e., the standard deviation $\pm\sigma_{\mathbf{X}\text{post}}(r_g(\lambda_{1,2}))$, returned by the inversion package on the diagonal of the a posteriori covariance matrix are reported with vertical bars. The horizontal dotted (dashed) lines correspond to maximum likelihood of the a priori PDF for the broadband visible (near-infrared) spectral domain.

values larger than approximately unity. The retrieval of LAI, especially for large values, remains indeed quite uncertain when using two spectral BHR values only in the measurement set even if the later is associated with a somewhat high accuracy level. Given the poor a priori knowledge specified with a constant LAI_{prior} value equal to 1.50 together with a large uncertainty, i.e., $\sigma_{\mathbf{X}\text{prior}}(LAI) = 5$, the knowledge gain from this inversion exercise, i.e., $\sigma_{\mathbf{X}\text{post}}(LAI)/\sigma_{\mathbf{X}\text{prior}}(LAI)$, is still remarkable. The second interesting feature concerns the impact on the retrieved distributions of LAI because of the slight differences occurring between the MODIS and MISR broadband BHR values, especially when low vegetation conditions are prevailing, i.e., mostly before and after the start of the growing and senescent periods. These differences (such as those observed in the broadband visible domain where MODIS BHRs are slightly lower than the corresponding MISR products) translate into MODIS LAI values (the maximum likelihood of the distributions) being systematically biased high (by about 0.5 absolute) with respect to those retrieved from MISR. In most cases, however, the PDFs of the MODIS and MISR LAI values share a significant common area as is illustrated by the overlapping of the uncertainty bars reported in Figure 6.

4.2. The Spectrally Variant Background Albedo

[37] The two-stream model implements solutions estimating the radiant fluxes on the basis of effective parameter values that characterize the vegetation layer, while, by contrast, the lower boundary condition is specified as the "true" value. Figure 7 displays the results of the retrievals regarding the background albedo values. The inversion procedure tolerates very significant departures from the mean a priori value as can be seen notably in the case of Dahra where rather bright background values are retrieved with, in most instances, high confidence levels. As discussed already in section 3.1, the background albedo returns to its a priori value, together with an increasing uncertainty range, in both spectral domains under conditions where LAI is large enough, i.e., during the summer period over the sites of Agro and Konza. In the case of Mongu, the retrievals feature a weak but systematic seasonal linear trend, partly arising because of correlations between the LAI and the soil background brightness. It is noteworthy that in situ

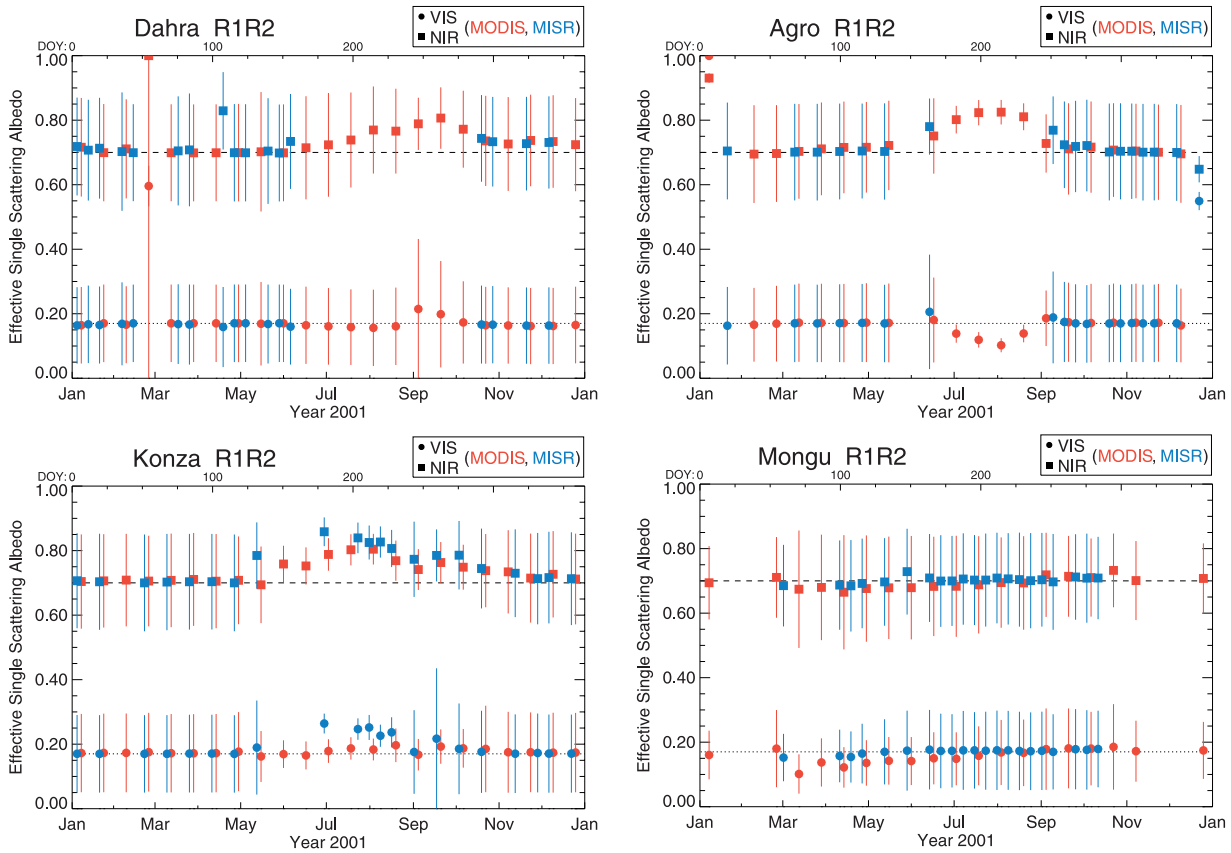

Figure 8. Same as Figure 7, except for the case of the effective single scattering albedo.

measurements mention a value of roughly 0.06 [*Huemmrich et al.*, 2005] for the soil background in the visible spectral domain which thus agrees well with the range of our retrievals over this site.

4.3. The Spectrally Variant Single Scattering Albedo

[38] As discussed in section 3.1, very limited knowledge is gained on the effective single scattering albedo when low LAI values occur (see Figure 8). Since the former parameter controls a large part of the measured BHRs when the vegetation becomes denser, the inversion procedure delivers $\omega_{\lambda(1,2)}$ values within a small uncertainty range. This result suggests that the deviations from the true single scattering albedo remain somewhat limited as can be anticipated for more closed/dense canopies. During the summer period over Konza, the MISR optimized values are also larger than those retrieved from MODIS in order to balance for the slight differences in the BHRs derived from these two instruments. The large single scattering values in both spectral domains (associated with a huge uncertainty range) occurring at the end of February over Dahra are accompanied by an abnormally high (with respect to the time series) cost function value for that particular 16-day period (see Figure 5). Somewhat analogous behaviors are observed at the very beginning and end of the year over the site of Agro where snow or frost conditions may have occurred. Note that the current setup of the inversion procedure is such that the snow background conditions are too unlikely to occur in the a priori knowledge (see Table 1) for being accepted as a solution within a good-enough confidence level. These are typical situations where adopting a temporally coupled inversion approach may prove beneficial.

4.4. The A Posteriori Absorbed Radiant Fluxes

[39] The PDFs of all radiant fluxes which the two-stream model is able to simulate can be delivered by the inversion procedure [see equation (3)]. Figures 9 and 10 show the estimated seasonal variations of the fraction of absorbed flux in the broadband visible A_1 (close to the green FAPAR) and near-infrared domains A_2, respectively. In the visible domain, dominated by single scattering regime, the effective LAI is the main driver for the absorption process, and, consequently, features observed on the retrieved LAI (see Figure 6) are duplicated on the absorbed fraction of radiation. These include the seasonality of the flux, the associated uncertainty values, and the bias, the magnitude of which is approximately 0.2, induced by small differences in the MODIS versus MISR BHRs mainly occurring at the beginning and at the end of the vegetation growing season. Analogous variations, although somewhat attenuated, are observed in the near-infrared domain especially when multiple scattering processes are becoming significant (for example, occurrence of bright background with substantial amount of leaves). Despite the relatively limited leaf absorption capability, a significant amount of incoming radiation still has a high probability of being absorbed by the canopy in the near-infrared domain.

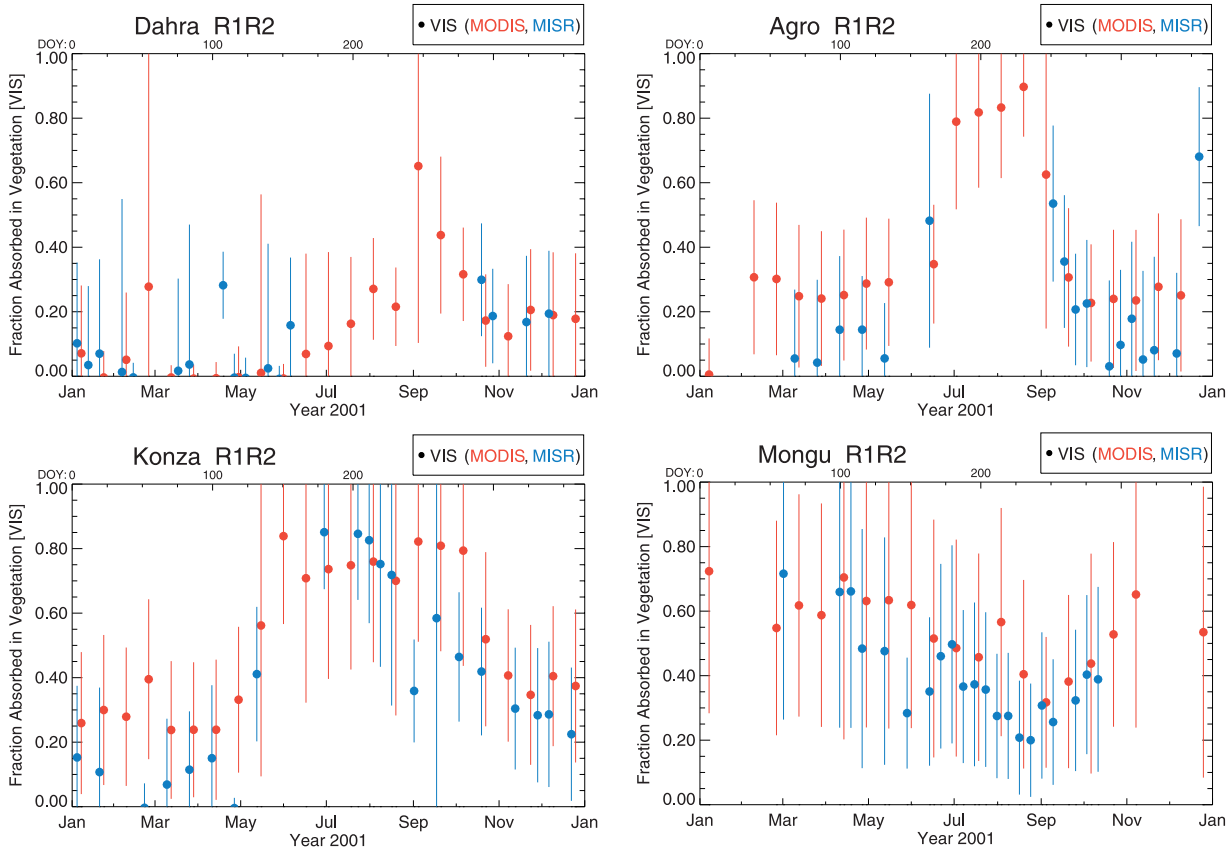

Figure 9. Time series of the fraction of absorbed radiation in the vegetation layer in the broadband visible domain (A_1) retrieved from the MODIS (red color) and MISR (blue color) BHR-white sky albedo products over the site of Dahra (top left panel), Agro (top right panel), Konza (bottom left panel), and Mongu (bottom right panel), respectively. A short description of the sites is provided in Table 2. MODIS (MISR) values are plotted on day 8 (4) of every 16-day (8-day) period. The standard deviations associated with the PDF of the retrieved values are reported with vertical bars.

[40] The joint estimation of the fraction of radiation which is scattered by, absorbed in, and transmitted through the canopy layer permits us deriving the fraction absorbed in the ground (below the vegetation layer). This later fraction estimated in the visible and near-infrared domain is depicted in Figures 11 and 12, respectively. The fractions absorbed in the ground in both spectral domains are about the same or slightly lower in the near infrared (for example, over the site of Dahra), with a smaller uncertainty in the near infrared as well. The seasonal trends follow quite logically those observed notably in the values of the effective LAI since the later largely controls the absorbed and scattered fractions. On average of the entire year and despite the ecological variability between the four midlatitude studied sites, the fraction of radiation absorbed in the ground is roughly around 0.5 of the amount available at the top of the vegetation canopy.

5. Toward Reducing Uncertainties

[41] Results presented in section 4 examples using Terra albedo products based on current operational products from Terra are characterized by very large uncertainty ranges on the LAI and the fraction of absorbed flux in the vegetation. As mentioned previously, these large uncertainty ranges arising when medium to high LAI conditions prevail are an immediate consequence of both the radiation transfer processes and the limited information provided in the a priori knowledge (see *Lavergne et al.* [2006] for results from a detailed analysis of the performances of the inversion package). These limitations include notably the uncertainty range specified on the albedo measurements as well as the width of the a priori distributions of the model parameter values. At this stage, one additional possibility to retrieve more accurate information on the model parameters consists in incorporating more measurements than the BHR-white sky albedos only. Given the nature of the radiation transfer processes in vegetation canopies (for instance, the fact that the LAI largely controls the fraction of absorbed radiation in the visible domain) together with results discussed in section 3, the inclusion of operational FAPAR products in the measurement configuration is thus quite appropriate. The specific SeaWiFS FAPAR products, delivered by the EC-Joint Research Centre (JRC), have been selected in the current application, instead of those from the Terra sensors, in order to limit as much as possible the correlation of uncertainties between the set of products incorporated in the measurement configuration. Such correlated uncertainties on the measurements can be handled

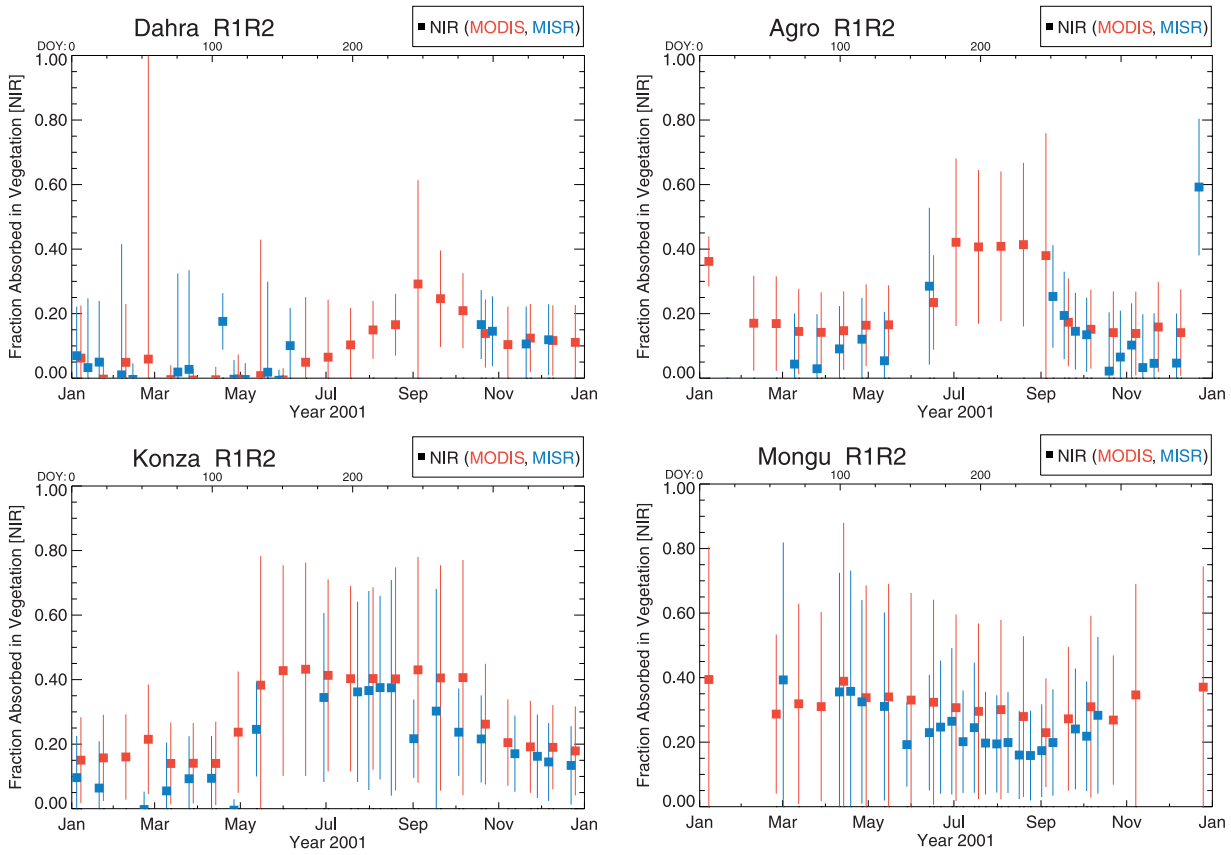

Figure 10. Same as Figure 9, except for the case of the fraction of absorbed radiation in the vegetation layer in the broadband near-infrared domain (A_2).

by our inverse procedure, but this would primarily increase the a posteriori uncertainties.

[42] The SeaWiFS FAPAR products are generated at JRC thanks to a dedicated processing chain that was developed to deliver daily, 10-day, and monthly time composite products at a global scale with spatial resolutions ranging from about 2 km up to 0.5° [*Mélin et al.*, 2002]. Accordingly, 7 years of SeaWiFS FAPAR products are available since the beginning of the mission in September 1997 [*Knorr et al.*, 2005]. The FAPAR algorithm was originally designed and implemented in order to generate, at medium spatial resolution, and from the set of radiances measured, at the top of the atmosphere for Sun angle conditions not exceeding 50–60°, in a blue, red, and near-infrared band, FAPAR products whose absolute accuracy remains statistically within the prespecified ±0.1 range. Results from the first attempts to validate these vegetation FAPAR products within this prespecified accuracy range are discussed in the study of *Gobron et al.* [2006]. The values of these products are function of the Sun angle at time of acquisition, and this angular dependency is accounted for in the current inversion procedure. It is noteworthy that FAPAR products may, in some instances, be lower than the total fraction of absorbed flux A_1, as understood by the two-stream model, notably because of the contributions due to nongreen and woody elements in the canopy.

[43] In order to deliver conservative estimates of uncertainties on the retrievals, a standard deviation value of 0.2 was specified for the fraction of absorbed flux A_1 in the covariance matrix $\mathbf{C}_d$.

5.1. Leaf Area Index

[44] The reduction in the uncertainty range on the retrievals of the effective LAI is quite significant for all studied cases, as can be seen from comparing results shown in Figures 13 and 14 (measurement configuration labeled $R_1R_2A_1$) with those discussed from Figure 6 (measurement configuration labeled R_1R_2). For LAI values larger than unity, the uncertainty is reduced by a factor of about 3 on average over all sites.

[45] Estimations of LAI values available over each site, from ground-based measurements (black thick pluses) as well as operational algorithms implemented for interpreting the MODIS (8-day composite values from collection 4, red thick crosses) and MISR (collection 6, blue thick crosses) surface bi-directional reflectance factors, are also shown in Figures 13 and 14. For the sake of readability of the figure, the expected uncertainty ranges on these products are not reported here. Note also that the operational LAI algorithms implemented on the Terra sensors intend at retrieving the "true" by contrast to the "effective" LAI [*Knyazikhin et al.*, 1998a, 1998b].

[46] The overall agreement between our two-stream-based retrievals using the MODIS white sky albedo (red diamonds) or the MISR BHRs (blue diamonds) and the ground-based estimations appears quite satisfactory for all four sites, given the many issues and caveats to be

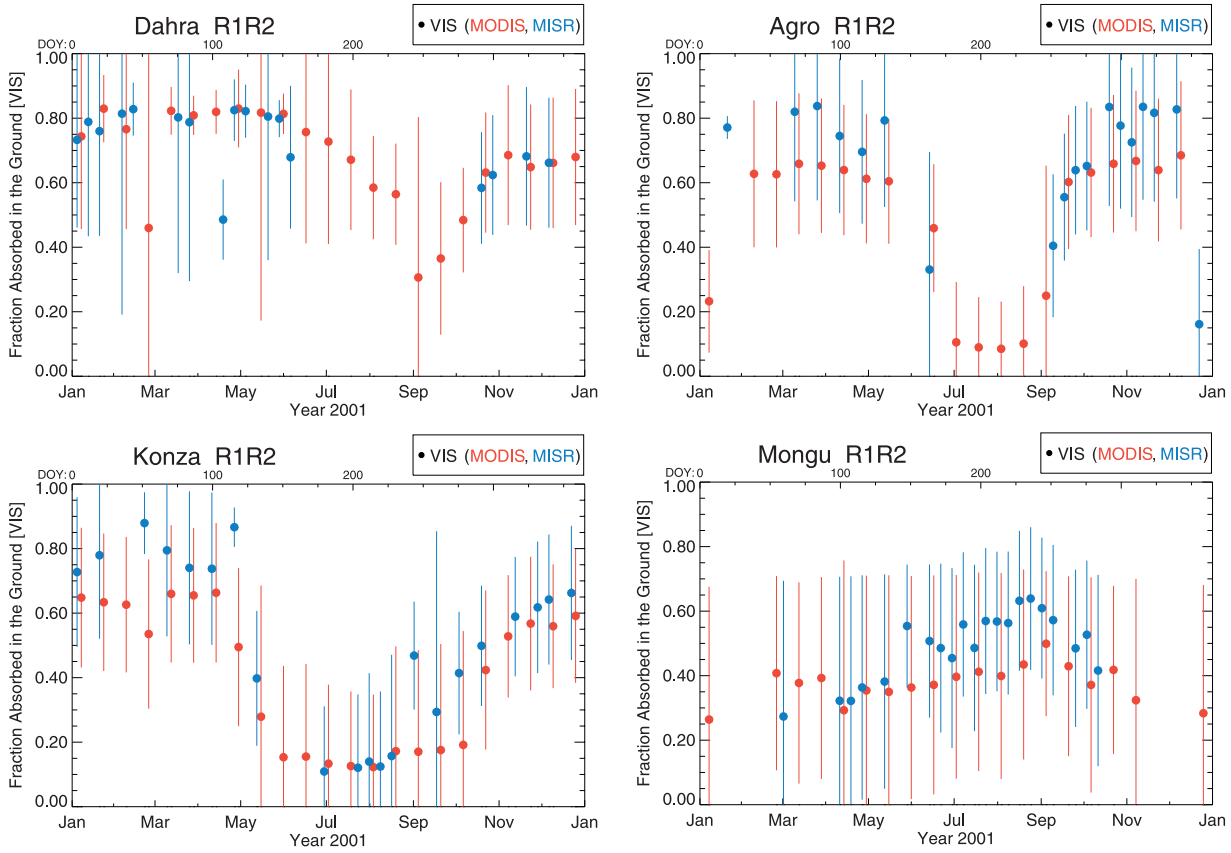

Figure 11. Same as Figure 9, except for the case of the fraction of absorbed radiation in the ground (below the vegetation layer) in the broadband visible domain.

addressed when interpreting the latter data sets at mesoscale spatial resolutions [e.g., *Morisette et al.*, 2005]. Note also that the ground-based estimations reported over the sites of Agro and Konza are for year 2000 [*Turner et al.*, 2004]. The in situ LAI values over Mongu correspond to effective LAI and include the additional contribution by about 0.3 from woody material [*Huemmrich et al.*, 2005, section 4.3]. One may also notice that the signature of the impact of the small differences discussed previously between the MODIS and MISR BHR values is also somewhat concealed with the current ($R_1R_2A_1$) measurement configuration.

[47] The diversity in vegetation phenology observed over all sites and depicted by the seasonal trends in LAI, such as the start, end, and length of the growing season, are well retrieved by the various analyses of the remote-sensing products. It is worthwhile to emphasize here that these analyses use different approaches, tools, and even input products; for example, the operational algorithms for the Terra sensors are based on spectral BRF information, while ours make use of broadband BHRs or white sky albedos eventually coupled with the SeaWiFS JRC-FAPAR products.

[48] The MODIS LAI operational product (from collection 4, with QA values equal to 0 and 1 only) is generally biased high with respect to both our current and ground-based estimations as well. This corroborates earlier findings reported over a variety of sites when comparing the successive MODIS LAI product collections against in situ derived values [see, e.g., *Fensholt et al.*, 2004; *Huemmrich et al.*, 2005; *Yang et al.*, 2005]. Part of this bias when occurring for low LAI conditions, for example, periods outside the range of the growing seasons, may be caused by slight differences in the input surface products. Our findings discussed in Figure 6 indeed suggest that these differences translate into LAI differences that may reach 0.5 under such geophysical situation. The MISR LAI operational algorithm delivers product values (collection 6) for a limited fraction of the time series over the four sites and this, even where and when valid surface BHR information exists. When this product is available, it does not exhibit any significant bias as is the case for MODIS, but in some instances, it shows a large temporal variability and can raise to unrealistically high values, for example, over the site of Mongu during the wet season.

[49] The absolute difference between the MODIS and MISR LAI operational products, estimated using a 16-day aggregation procedure, is equal to 0.82, on average over the year and over the four selected sites. By comparison, the average difference obtained with our inversion procedure using the MODIS white sky and MISR BHR values only, i.e., the R_1R_2 measurement configuration, does not exceed 0.28, i.e., a reduction by a factor of about 3 with respect to the operational products. Given that the same algorithm operated with the same type of measurements was applied on both instruments, this value of 0.28 quantifies the impact to be expected on the LAI product because of slight differences between the MODIS and MISR surface albedo products. Logically, this difference is further reduced to

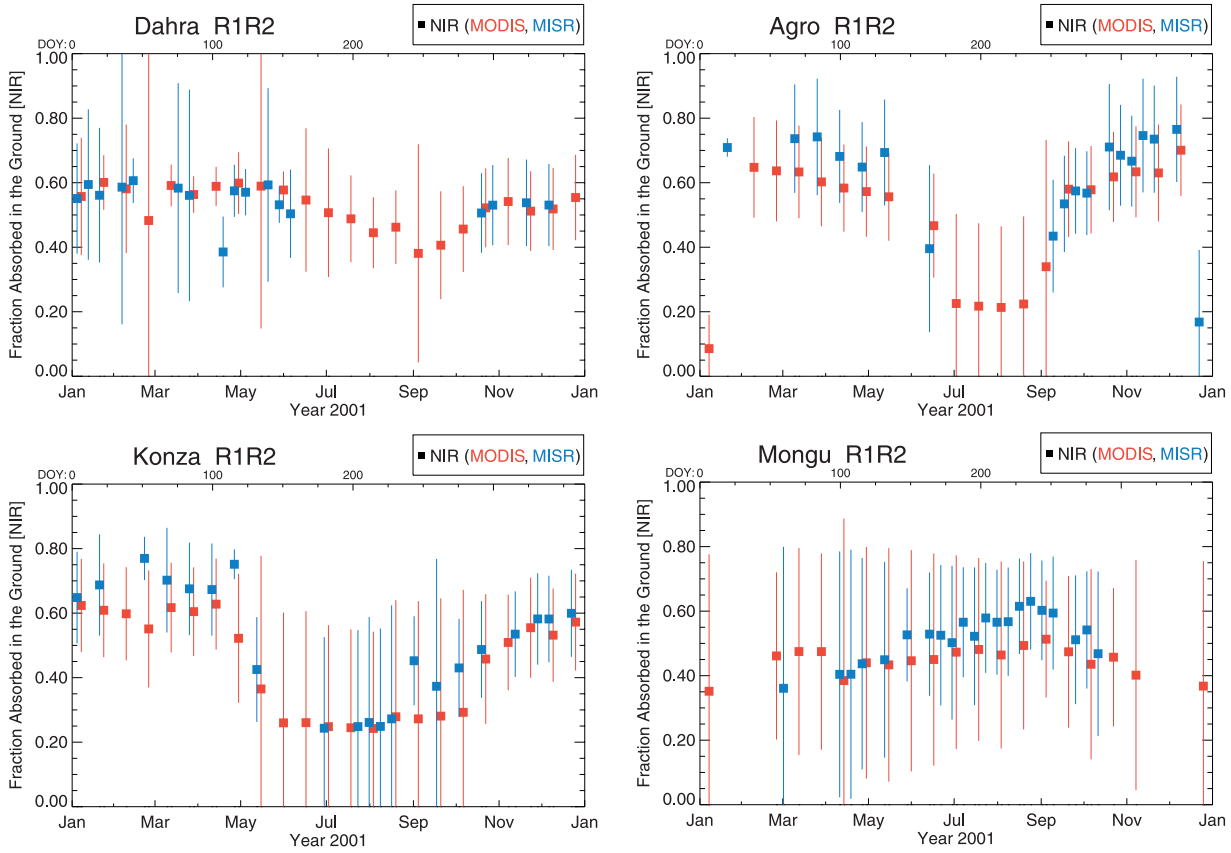

Figure 12. Same as Figure 10, except for the case of the fraction of absorbed radiation in the ground (below the vegetation layer) in the broadband near-infrared domain.

0.14 when operating the inversion package with the $R_1R_2A_1$ measurement configuration.

5.2. Fraction of Absorbed Radiation in the Visible Domain

[50] The inversions performed with the measurement configuration $R_1R_2A_1$ generate model parameter values which are close to those discussed in section 4 examples using Terra albedo products. This updated set of parameter values can then be adopted to estimate the a posteriori radiant fluxes as proposed in section 4.4, including the instantaneous fraction absorbed by the vegetation $A_1(\mu_0)$ considered here as equivalent or indiscernible to the FAPAR products. The benefit from reducing the uncertainty ranges on the retrieval of the effective LAI is illustrated in Figures 15 and 16, showing the corresponding fraction of absorbed radiation by the vegetation layer in the broadband visible domain, at time of acquisition by the SeaWiFS sensor. This fraction is indeed associated with much lower uncertainty range than when solving the inverse problem using the MODIS and/or MISR BHR information only (see Figure 9).

[51] Comparing the original (shown in green symbols in Figures 15 and 16) and the a posteriori FAPAR values [shown in red (blue) symbols when coupled with the MODIS (MISR) BHRs] reveals notably the following:

[52] ● The two sets of products remain close to each other in the vast majority of cases. In other words, the inverse problems could be solved without requiring drastic corrections to the a priori FAPAR values.

[53] ● In a few instances generally associated with low vegetation density, as is the case over Dahra at DOY 110, showing suspiciously low MISR BHR value in the visible domain (Figure 5), the strong constraint imposed by the BHRs forces the FAPAR to take on values probably lying out of the range that can be expected when considering the full time series. Such undesirable events could be avoided by increasing the uncertainty on these BHR values and/or applying the inversion for a time series of acquisition.

[54] ● The a posteriori covariance matrix delivered by the inversion allows us to refine the uncertainty range on our measurements, such as the FAPAR. In a number of cases, the standard deviation values $\pm\sigma_{d_{post}}$(FAPAR) is smaller than the corresponding a priori values (set at ±0.2).

[55] The order of magnitude of our current estimates compares favorably over those sites where ground-based estimations of FAPAR are available. One must keep in mind here the significant levels of difficulty to be faced for deriving accurately and reliably such flux domain-averaged quantities [e.g., *Gobron et al.*, 2006; *Widlowski et al.*, 2006; *Yang et al.*, 2005]. Over the sites of Agro and Konza, the ground-based FAPAR estimations are derived assuming an exponential attenuation given by the Beer's law with extinction coefficients of 0.58 and 0.5, respectively [*Turner et al.*, 2004]. In these instances, the reported FAPAR values are thus a one-to-one function/rescaling of the in situ LAI estimations. In the case of Mongu, the measurement protocols for the effective LAI and FAPAR involve different instruments and procedures. Incidentally, one may notice

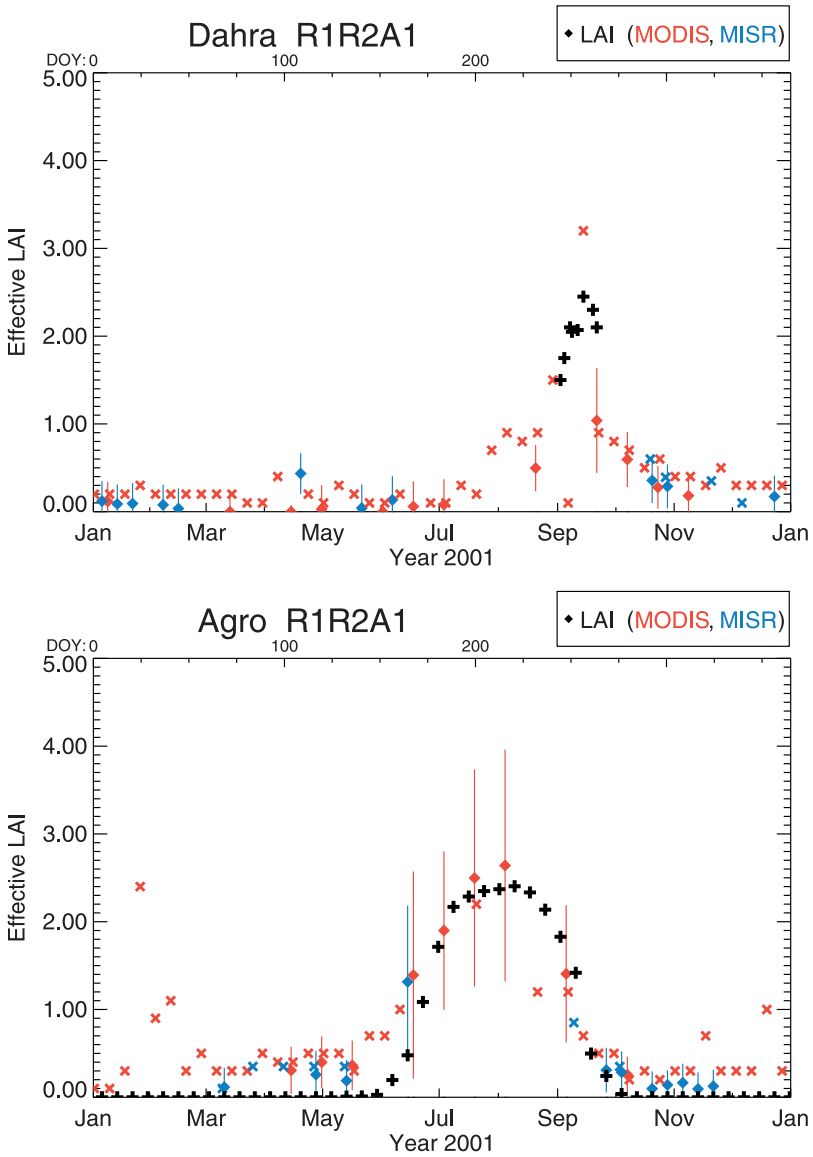

Figure 13. Time series of the effective leaf area index (LAI) retrieved by our inversion procedure (symbols ●) from the MODIS (in red color) and MISR (in blue color) BHR-white sky albedo products over the site of Dahra (top panel) and Agro (bottom panel), respectively. MODIS (MISR) values are plotted on day 8 (4) of every 16-day (8-day) period. The associated uncertainty values, i.e., $\pm\sigma_{\mathbf{X}_{\mathrm{post}}}(\mathrm{LAI})$, are reported with vertical bars. Symbols (×) indicate the retrievals from the MODIS (in red color) and MISR (in blue color) operational algorithms, respectively, while the black color pluses (+) refer to the ground-based estimations.

that the good agreement observed between the in situ and remote-sensing-derived LAI product (see bottom right panel on Figure 6) tends to deteriorate during the wet season, in the case of the FAPAR products only.

[56] The bias toward high values noticed previously from the MODIS LAI operational product is exhibited as well by the MODIS FAPAR product. There is no analogous bias when considering the FAPAR product generated by the MISR operational algorithm, but the large temporal variability mentioned earlier is still significant. The annual average over the four sites of the absolute difference between the MODIS and MISR FAPAR operational products is equal to 0.17, with a maximum of 0.23 occurring over Mongu. This difference decreases to a value of 0.11, with a maximum of 0.15 occurring over Konza, when applying our two-stream inversion package with the MODIS white sky and MISR BHR values only, i.e., the R_1R_2 measurement configuration.

6. Conclusions

[57] The availability of multiannual radiant flux products derived operationally over land surfaces at the global scale from various institutions encourages their exploitation for general climate model applications. Achieving this objective requires to ensure the physical consistency between

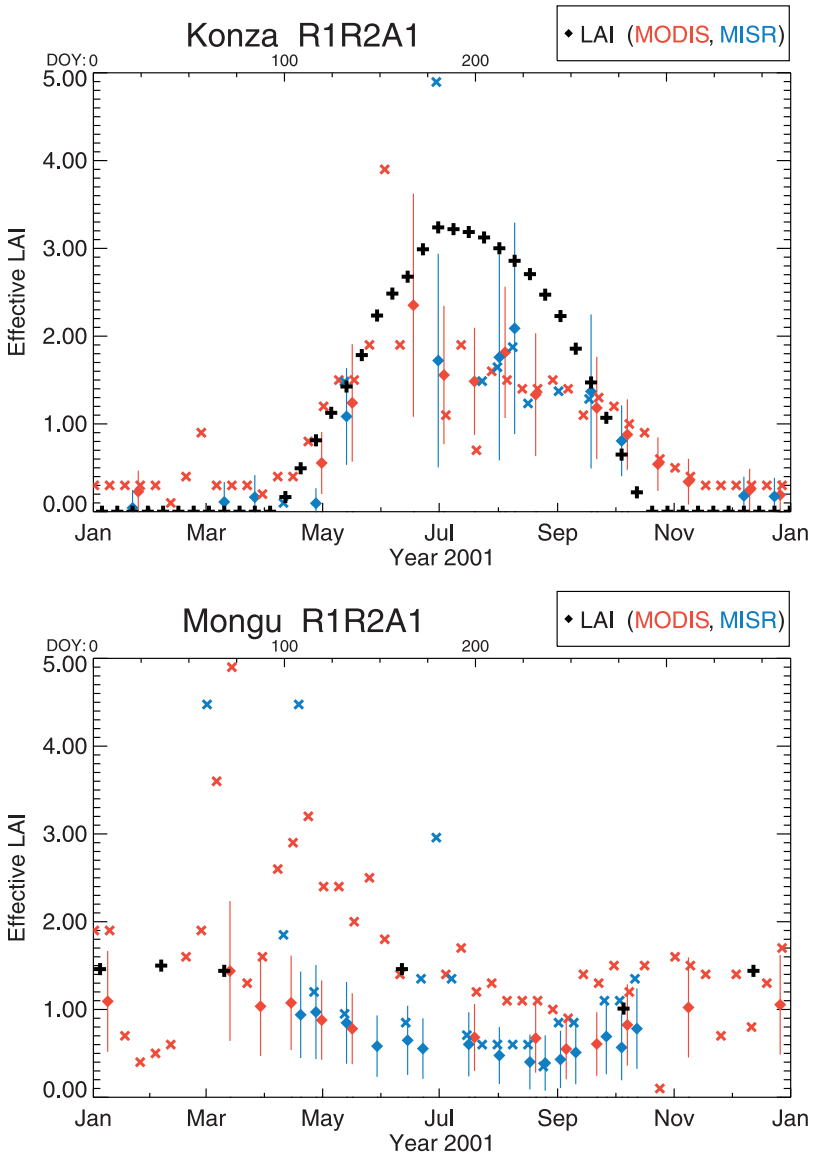

Figure 14. Same as Figure 13, except for the case of the Konza and Mongu sites.

these radiant flux products such as albedos and the associated values of the state variables entering the one-dimensional or two-stream representation of the radiation transfer regime in general climate models. To remedy this situation, *Pinty et al.* [2006] have suggested, for instance, that effective instead of allometric LAI values must be considered for ingestion by general climate models in order to generate the correct balance between the fluxes reflected, absorbed, and transmitted by vegetation canopy layers. As a consequence, radiant flux products derived from remote-sensing measurements must be analyzed in order to retrieve the desired state variables, which are effective values for those characterizing the vegetation layer but true values for the soil underneath.

[58] The proposed methodology which is developed and tested in the present contribution capitalizes on advanced software techniques, such as automatic differentiation used to generate the adjoint and Hessian code of a cost function. This software package inverts the two-stream model of *Pinty et al.* [2006] in a numerically accurate and computer-efficient manner. It delivers extensive statistical information on the results, allowing us to evaluate in quantitative terms the quality of the retrievals and the performance of the inverse procedure itself. The procedure thus delivers estimates of the PDFs of all variables entering the two-stream model and all the radiant fluxes that can be generated by this model. Correlations are assessed from the a posteriori covariance matrix. The inverse package can be operated using various measurement configurations including those with a limited number of radiant fluxes, for example, the broadband visible and near-infrared reflected fluxes only in the solar domain.

[59] A series of tests have been conducted using two-stream model-based simulated scenarios. It was shown, for instance, that the agreement between the series of true LAI values and those retrieved by inversion is remarkable. The associated uncertainties remain within a quite small range $[\sigma_{\mathbf{X}_{\text{post}}}(LAI) \approx 0.35 \times \text{LAI}_{\text{post}}]$ for all canopy conditions

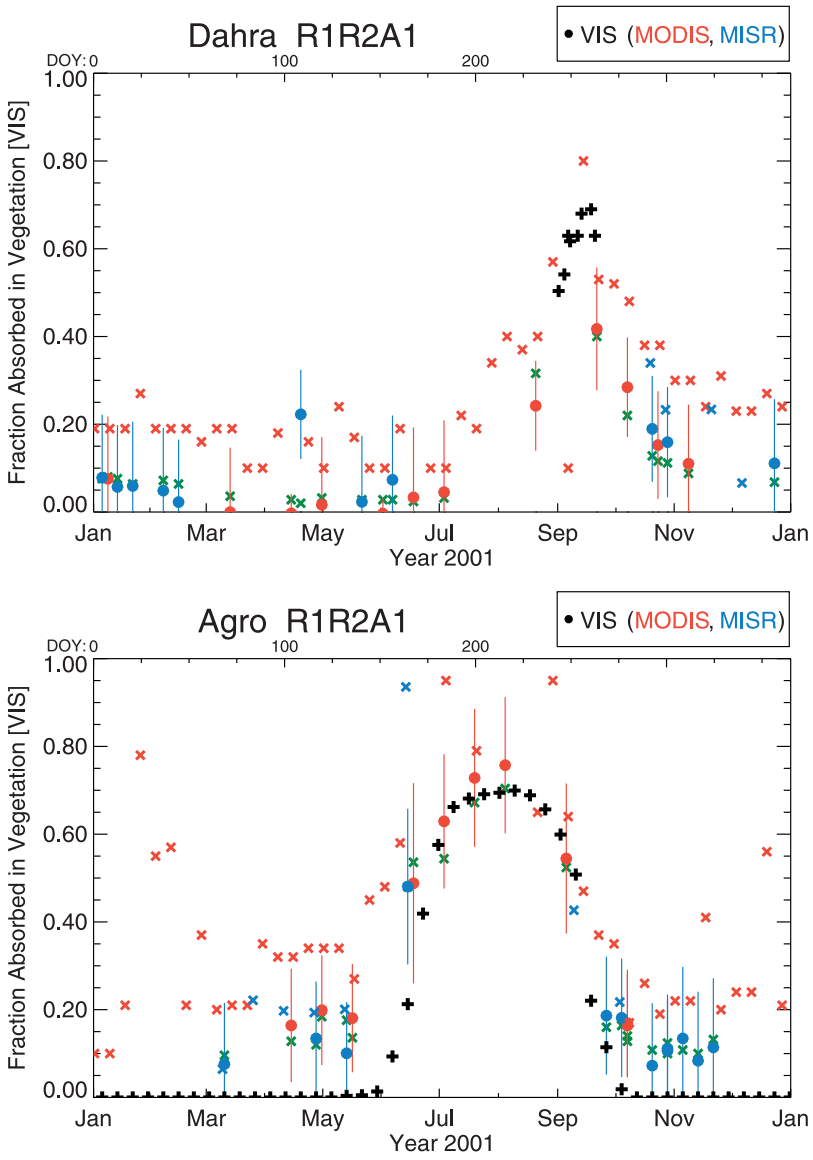

Figure 15. Time series of the fraction of absorbed radiation in vegetation in the broadband visible domain (A_1) retrieved by our inversion procedure (symbols ●) from the MODIS (in red color) and MISR (in blue color) BHR-white sky albedo products over the site of Dahra (top panel) and Agro (bottom panel), respectively. MODIS (MISR) values are plotted on day 8 (4) of every 16-day (8-day) period. The standard deviations associated with the PDFs of the retrieved values are reported with vertical bars. Symbols (×) indicate the retrievals from the MODIS (in red color), MISR (in blue color), and SeaWiFS (in green color) operational FAPAR algorithms, respectively, while the black color pluses (+) refer to the ground-based estimations.

where the a posteriori LAI values are less than 4.0. This uncertainty range is obtained under rather favorable measurement conditions that include the visible and near-infrared broadband BHRs (associated with a 5% relative uncertainty) together with the fraction of absorbed flux in the visible domain (associated with a 0.1 absolute uncertainty). The knowledge gain on the model process parameters thanks to the inversion is appreciated by comparing the a posteriori with the a priori uncertainty estimates.

[60] The inverse methodology has been applied over four selected midlatitude EOS validation sites representing a large variety of surface conditions regarding the vegetation type and phenology, as well as the three-dimensional heterogeneity. This application was performed first using the visible and near-infrared broadband BHRs (or white sky albedos) generated from data acquired by the MODIS and MISR instruments on board the Terra platform. The retrievals of all the two-stream model variables were successful and, in some instances, could be compared favorably with available ground-based estimations. These retrievals were then used to derive a posteriori estimates of radiant flux quantities and their associated uncertainties, including fluxes not directly observed such as the fraction of solar radiation absorbed in the ground below the vegetation layer.

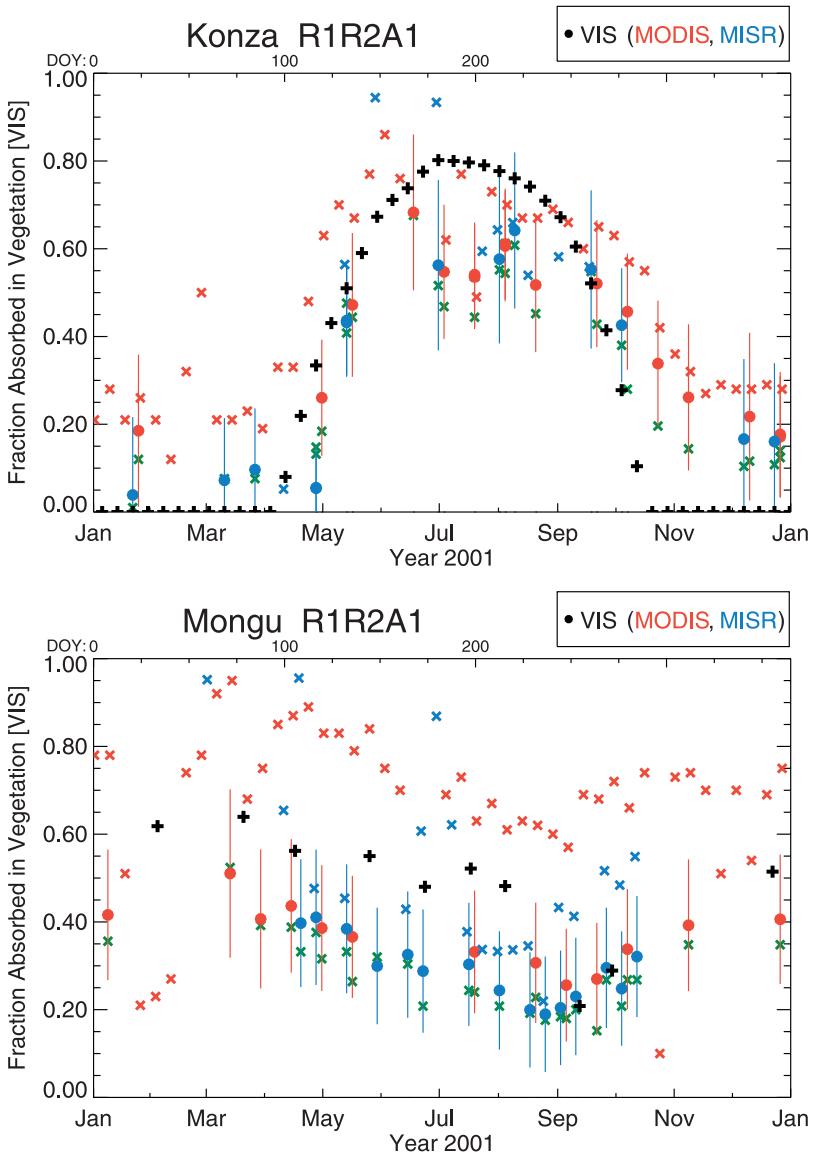

Figure 16. Same as Figure 15, except for the case of the Konza and Mongu sites.

This analysis reveals the sensitivity of the maximum likelihood estimator of LAI and the fraction of the absorbed flux by vegetation under sparse vegetation canopy conditions to slight differences or biases existing between the MODIS and MISR BHR products. It also demonstrates the large uncertainty levels associated with the retrievals. These are mainly a consequence of the limited a priori knowledge on the model parameters and the available measurement set. One simple way to remedy this situation consists in adding extra measurements in order to increase the a priori knowledge on the geophysical system under study. This was achieved using the Terra-independent estimates of the FAPAR, produced at the Joint Research Centre on the basis of the data acquired globally by the SeaWiFS sensor. The JRC-FAPAR SeaWiFS products were included in the measurement set that is used together with the MODIS and MISR BHRs, with an absolute uncertainty of 0.2.

[61] The analysis of this second set of inversion results yields the following main conclusions:

[62] • The uncertainty levels on the estimates of all model parameters and related radiant fluxes are significantly reduced.

[63] • The slight differences existing between the input MODIS and MISR BHRs do not translate into discernible signatures on the retrievals.

[64] • The time series of the retrieved quantities are quite smooth and exhibit, in all canopy conditions, much less variability than those derived by the operational MODIS and MISR algorithms, although all the inversions were performed here in independently with respect to time.

[65] • The retrieved quantities (model parameters and fluxes) are in very good agreement with ground-based estimates, even over the radiatively complex situation prevailing at the Mongu site.

[66] The proposed inverse methodology thus provides an efficient and practical way to generate, by reanalyzing the existing radiant flux products at limited cost, a consolidated and unique Terra series of land surface products especially devoted to large-scale and climate model applications. Upcoming research efforts will concentrate on challenging conditions such as those encountered at high latitudes over boreal forest systems where contamination by snow remains an issue. The proposed methodology implements, however, all basic ingredients required to perform the assimilation of the remote-sensing flux products in a temporally coupled mode that could prove useful under these challenging conditions.

[67] **Acknowledgments.** The authors gratefully acknowledge the contribution from M. Robustelli and F. Mélin. The authors would like to thank the support of all the providers of the remote-sensing and ground-based data sets needed to perform this research. The MISR products were obtained from the NASA Langley Research Center Atmospheric Sciences Data Center. The MODIS products were obtained from the NASA Land Processes Distributed Active Archive Centers. The authors also thank the Ocean Biology Processing Group and the Distributed Active Archive Center at the NASA Goddard Space Flight Center for the distribution of the SeaWiFS data. This research would not have been possible without the support of the Global Environment Monitoring unit of the Institute for Environment and Sustainability at the DG Joint Research Centre, an institution of the European Commission.

References

Anisimov, O., and L. Fukshansky (1992), Stochastic radiation in macroheterogeneous random optical media, *J. Quant. Spectrosc. Radiat. Transfer*, *48*, 169–186.

Davis, A. B., and A. Marshak (2004), Photon propagation in heterogeneous optical media with spatial correlations: Enhanced mean free-paths and wider-than-exponential free-path distributions, *J. Quant. Spectrosc. Radiat. Transfer*, *84*, 3–34.

Dickinson, R. E. (1983), Land surface processes and climate—Surface albedos and energy balance, *Adv. Geophys.*, *25*, 305–353.

Dickinson, R. E., A. Henderson-Sellers, P. J. Kennedy, and M. F. Wilson (1986), Biosphere Atmosphere Transfer Scheme (BATS) for the NCAR Community Climate Model, *Technical Note TN275+STR*, National Center for Atmospheric Research.

Engelsen, O. B. Pinty M. M. Verstraete and J. V. Martonchik (1996), Parametric bidirectional reflectance factor models: Evaluation, improvements and applications, *Technical Report EUR 16426 EN*, EC Joint Research Centre.

Enting, I. G., C. M. Trudinger, and R. J. Francey (1995), A synthesis inversion of the concentration and $\delta^{13}C$ of atmospheric CO_2, *Tellus, Ser. B*, *47*, 35–52.

Fensholt, R., I. Sandholt, and M. S. Rasmussen (2004), Evaluation of MODIS LAI, fAPAR and the relation between fAPAR and NDVI in a semi-arid environment using in situ measurements, *Remote Sens. Environ.*, *91*, 490–507.

Giering, R., and T. Kaminski (1998), Recipes for adjoint code construction, *ACM Trans. Math. Software*, *24*, 437–474.

Gobron, N., B. Pinty, and M. M. Verstraete (1997), Theoretical limits to the estimation of the leaf area index on the basis of optical remote sensing data, *IEEE Trans. Geosci. Remote Sens.*, *35*, 1438–1445.

Gobron, N., et al. (2006), Evaluation of FAPAR products for different canopy radiation transfer regimes: Methodology and results using Joint Research Centre products derived from SeaWiFS against ground-based estimations, *J. Geophys. Res.*, *111*, D13110, doi:10.1029/2005JD006511.

Govaerts, Y., B. Pinty, M. Taberner, and A. Lattanzio (2006), Spectral conversion of surface albedo derived from Meteosat First Generation observations, *IEEE Geosci. Remote Sens. Lett.*, *3*, 23–27, doi: 10.1109/LGRS.2005.854,202.

Griewank, A. (2000), Evaluating Derivatives: Principles and Techniques of Algorithmic Differentiation, 369 pp., Frontiers in Applied Mathematics 19, SIAM, Philadelphia.

Huemmrich, K. F., J. L. Privette, M. M. Mukelabai, R. B. Myneni, and Y. Knyazikhin (2005), Time-series validation of MODIS land biophysical products in a Kalahari woodland, Africa, *Int. J. Remote Sens.*, *26*, 4381–4398.

Jin, Y., C. B. Schaaf, C. E. Woodcock, F. Gao, X. Li, and A. H. Strahler (1999), Consistency of MODIS surface bidirectional reflectance distribution function and albedo retrievals: 2. Validation, *J. Geophys. Res.*, *108*(D5), 4159, doi:10.1029/2002JD002804.

Kaminski, T., M. Heimann, and R. Giering (1999), A coarse grid three-dimensional global inverse model of the atmospheric transport: 2. Inversion of the transport of CO_2 in the 1980s, *J. Geophys. Res.*, *104*, 18,555–18,581.

Kaminski, T., R. Giering, M. Scholze, P. Rayner, and W. Knorr (2003), An example of an automatic differentiation-based modelling system, in Computational Science—ICCSA 2003, International Conference Montreal, Canada, May 2003, Proceedings, Part II, pp. 95–104, Springer, New York.

Knorr, W., N. Gobron, M. Scholze, T. Kaminski, and B. Pinty (2005), Global-scale drought caused atmospheric CO_2 increase, *Eos Trans. AGU*, *86*, 178–181.

Knyazikhin, Y., J. V. Martonchik, D. J. Diner, R. B. Myneni, M. M. Verstraete, B. Pinty, and N. Gobron (1998a), Estimation of vegetation canopy leaf area index and fraction of absorbed photosynthetically active radiation from atmosphere-corrected MISR data, *J. Geophys. Res.*, *103*, 32,239–32,256.

Knyazikhin, Y., J. V. Martonchik, R. B. Myneni, D. J. Diner, and S. W. Running (1998b), Synergistic algorithm for estimation of vegetation canopy leaf area index and fraction of absorbed photosynthetically active radiation from MODIS and MISR data, *J. Geophys. Res.*, *103*, 32,257–32,276.

Lavergne, T., M. Vossbeck, B. Pinty, T. Kaminski, and R. Giering (2006), Evaluation of the 2-stream model inversion package, EUR Report No. 22467 EN, Joint Research Centre Institute for Environment and Sustainability.

Lavergne, T., T. Kaminski, B. Pinty, M. Taberner, N. Gobron, M. M. Verstraete, M. Vossbeck, J.-L. Widlowski, and R. Giering (2007), Applications to MISR land products of an RPV model inversion package using adjoint and Hessian codes, *Remote Sens. Environ.*, *107*, 362–375.

Liang, S. (2000), Narrowband to broadband conversions of land surface albedo—I algorithms, *Remote Sens. Environ.*, *76*, 213–238.

Liang, S., A. H. Strahler, and C. Walthall (1999), Retrieval of land surface albedo from satellite observations: A simulation study, *J. Appl. Meteorol.*, *38*, 712–725.

Martonchik, J. V., D. J. Diner, B. Pinty, M. M. Verstraete, R. B. Myneni, Y. Knyazikhin, and H. R. Gordon (1998), Determination of land and ocean reflective, radiative, and biophysical properties using multiangle imaging, *IEEE Trans. Geosci. Remote Sens.*, *36*, 1266–1281.

Meador, W. E., and W. R. Weaver (1980), Two-stream approximations to radiative transfer in planetary atmospheres: A unified description of existing methods and new improvements, *J. Atmos. Sci.*, *37*, 630–643.

Mélin, F., C. Steinich, N. Gobron, B. Pinty, and M. Verstraete (2002), Optimal merging of LAC and GAC data from SeaWiFS, *Int. J. Remote Sens.*, *23*, 801–807.

Moody, E. G., M. D. King, S. Platnick, C. B. Schaaf, and F. Gao (2005), Spatially complete global spectral surface albedos, *IEEE Trans. Geosci. Remote Sens.*, *43*, 144–158.

Morisette, J. T., et al. (2005), Validation of global moderate resolution LAI products: A framework proposed within the CEOS Land Product Validation subgroup, *IEEE Trans. Geosci. Remote Sens.*, in print.

Niu, G.-Y., and Z.-L. Yang (2004), Effects of vegetation canopy processes on snow surface energy and mass balance, *J. Geophys. Res.*, *109*, D23111, doi:10.1029/2004JD004884.

Pinty, B., N. Gobron, J.-L. Widlowski, T. Lavergne, and M. M. Verstraete (2004a), Synergy between 1-D and 3-D radiation transfer models to retrieve vegetation canopy properties from remote sensing data, *J. Geophys. Res.*, *109*, D21205, doi:10.1029/2004JD005214.

Pinty, B. M., et al. (2004b), Intercomparison of surface albedo products from various spaceborne sensors, in Proceedings of the Workshop on Inter-comparison of Large Scale Optical and Infrared Sensors, ESA ESTEC, Noordwijk, Netherlands, 12–14 October 2004, ESA ESTEC.

Pinty, B., A. Lattanzio, J. V. Martonchik, M. M. Verstraete, N. Gobron, M. Taberner, J.-L. Widlowski, R. E. Dickinson, and Y. Goverts (2005), Coupling diffuse sky radiation and surface albedo, *J. Atmos. Sci.*, *62*(7), 2580–2591.

Pinty, B., T. Lavergne, R. E. Dickinson, J.-L. Widlowski, N. Gobron, and M. M. Verstraete (2006), Simplifying the interaction of land surfaces with radiation for relating remote sensing products to climate models, *J. Geophys. Res.*, *111*, D02116, doi:10.1029/2005JD005952.

Press, W. H., B. P. Flannery, S. A. Teulkosky, and W. T. Vetterling (1986), Numerical Recipes in C, 1st edition, Cambridge Univ. Press, New York.

Price, J. C. (1995), Examples of high resolution visible to near-infrared reflectance spectra and a standardized collection for remote sensing studies, *Int. J. Remote Sens.*, *16*, 993–1000.

Rayner, P. J., M. Scholze, W. Knorr, T. Kaminski, R. Giering, and H. Widmann (2005), Two decades of terrestrial carbon fluxes from a Carbon Cycle Data Assimilation System (CCDAS), *Global Biogeochem. Cycles*, *19*, GB2026, doi:10.1029/2004GB002254.

Salomon, J., C. B. Schaaf, A. H. Strahler, F. Gao, and Y. Jin (2006), Validation of the MODIS bidirectional reflectance distribution function and albedo retrievals using combined observations from the Aqua and Terra platforms, *IEEE Trans. Geosci. Remote Sens.*, in print.

Schaaf, C. B., et al. (2002), First operational BRDF, albedo and nadir reflectance products from MODIS, *Remote Sens. Environ.*, *83*, 135–148.

Sellers, P. J. (1985), Canopy reflectance, photosynthesis and transpiration, *Int. J. Remote Sens.*, *6*, 1335–1372.

Shabanov, N. V., Y. Wang, W. Buermann, J. Dong, S. Hoffman, G. R. Smith, Y. Tian, Y. Knyazikhin, and R. B. Myneni (2003), Effect of foliage spatial heterogeneity in the MODIS LAI and FPAR algorithm over broadleaf forests, *Remote Sens. Environ.*, *85*, 410–423.

Tarantola, A., (1987), Inverse Problem Theory, Methods for Data Fitting and Model Parameter Estimation, 630 pp., Elsevier, New York.

Tarantola, A., and B. Valette (1982), Generalized nonlinear inverse problems solved using the least square criterion, *Rev. Geophys. Space Phys.*, *22*, 219–232.

Turner, D. P., et al. (2004), Site-level evaluation of satellite-based global terrestrial GPP and NPP modeling, *Glob. Change Biol.*, *11*, 666–684.

Wang, S. (2005), Dynamics of surface albedo of a Boreal forest and its simulation, *Ecol. Model.*, *183*, 477–494.

Widlowski, J.-L., B. Pinty, T. Lavergne, M. M. Verstraete, and N. Gobron (2006), Horizontal radiation transport in 3-D forest canopies at multiple spatial resolutions: Simulated impact on canopy absorption, *Remote Sens. Environ.*, *103*, 379–397, doi:10.1016/j.rse.2006.03.014.

Yang, R., M. A. Friedl, and W. Ni (2001), Parameterization of shortwave radiation fluxes for nonuniform vegetation canopies in land surface models, *J. Geophys. Res.*, *106*(D13), 14,275–14,286.

Yang, W., et al. (2005), MODIS Leaf Area Index products: from validation to algorithm improvement, *IEEE Trans. Geosci. Remote Sens.*, in print.

O. Aussedat, N. Gobron, T. Lavergne, B. Pinty, M. Taberner, M. M. Verstraete, and J.-L. Widlowski, Global Environment Monitoring Unit, European Commission, DG Joint Research Centre, Institute for Environment and Sustainability, TP 440, via E. Fermi, I-21020, Ispra (VA), Italy. (bernard.pinty@jrc.it)

R. Giering, T. Kaminski, and M. Voßbeck, FastOpt, Schanzenstrasse 36, D-20357 Hamburg, Germany.